Catena 235 (2024) 107672

Contents lists available at ScienceDirect

Catena

journal homepage: www.elsevier.com/locate/catena

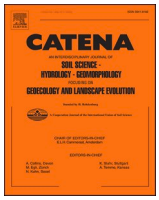

Natural radionuclides as tracers of coastal sediment dynamics in El Confital Bay (Spain): Spatial distribution and relationships with sediment characteristics

A.C. Arriola-Velásquez [a], A. Tejera [a,*], I. Alonso [b], F. Cámara [c], M. Cantaluppi [c], H. Alonso [a], N. Miquel-Armengol [a], J.G. Rubiano [a], P. Martel [a]

[a] Department of Physics, Instituto Universitario de Investigación en Estudios Ambientales y Recursos Naturales i-UNAT, Universidad de Las Palmas de Gran Canaria, Campus de Tafira, 35017 Las Palmas de Gran Canaria, Spain
[b] Instituto de Oceanografía y Cambio Global, IOCAG, Universidad de Las Palmas de Gran Canaria, Campus de Tafira, 35017 Las Palmas de Gran Canaria, Spain
[c] Dipartimento di Scienze della Terra, Università degli Studi di Milano, via Sandro Botticelli 23, 20133 Milano, Italy

ARTICLE INFO

Keywords:
Radionuclides
Tracer
Sediment dynamics
Coastal sediments
Grain size

ABSTRACT

Erosion and accumulation of coastal areas have become an increasing concern in recent years since they can result in important social and economic problems. In this framework, natural radionuclides have emerged as an alternative tool to study coastal sediment transport and help with the management of the littoral zone. However, there is still a lack of knowledge on how these radionuclides can be applied as tracers of coastal sediment dynamics and how the sediment characteristics can influence this use. Thus, a methodology is presented in this work to use natural radionuclides as tracers of coastal erosion, transport and accumulation of sediments. For this purpose, the spatial distributions of ^{226}Ra, ^{228}Ra, ^{40}K and unsupported ^{210}Pb (^{210}Pb$_{ex}$) in two periods of time were analysed and compared in a coastal area with diverse marine dynamics. The results showed that ^{226}Ra, ^{228}Ra and ^{40}K identified the different sediment erosion, transport and accumulation occurring in the study region. In addition, it was found that changes in the activity concentrations of the samples were mostly related to variations in their mineralogical composition. Finally, the activity concentration values of ^{210}Pb$_{ex}$ made it possible to trace the areas where accumulation due to the sedimentation of aerosol particles in the seabed is favoured. These results highlight the suitability of natural radionuclides to study coastal sediment transport.

1. Introduction

Uncontrolled sediment transport in the coastal environment can lead to considerable economic and social consequences. Some of these include long-term retreat of the shorelines that can result in beach losses and danger to coastal human settlements or the return to ports and harbours of material previously dredged from them affecting their navigation channels (International Atomic Energy Agency, 2014). In this framework, having tools to study the erosion, transport and accumulation of sediments in the environment is essential in order to obtain the necessary information for the building and maintenance of coastal and riverine infrastructures, as well as for the design of mechanisms for coastal protection such as barriers for beach and littoral protection.

In the past, artificial radionuclides were used to trace sediment erosion, transport and accumulation but, in recent years, natural radionuclides have emerged as better alternative tracers of coastal sediment dynamics since they do not require anthropogenic introduction in the system as they already belong to it (International Atomic Energy Agency, 2014). Most of these naturally occurring radionuclides are primordial radionuclides that can be found in the Earth's crust since its formation (like ^{40}K and those from the natural decay chains of ^{238}U, ^{232}Th and ^{235}U) and their activity concentrations in sediments are controlled by the natural geochemical characteristics of the original sediment sources (Froehlich, 2010). Therefore, changes in their activity concentrations in sediments from the same area are related to local physicochemical alterations including the transport of the sediment containing them.

In coastal areas, natural radionuclides, such as those from the ^{232}Th and ^{238}U series or ^{40}K have been used as tracers of different sedimentary processes. Some authors focused on the use of these radionuclides as

* Corresponding author.
E-mail address: alicia.tejera@ulpgc.es (A. Tejera).

https://doi.org/10.1016/j.catena.2023.107672
Received 16 February 2023; Received in revised form 30 October 2023; Accepted 3 November 2023
Available online 11 November 2023

tracers of sedimentation rates (Cooper and Grebmeier, 2018; Eulie et al., 2018; Tsabaris et al., 2012). Other studies used, among others, ^{232}Th, ^{238}U, ^{210}Pb or ^{40}K to evaluate sediment transport and sources in coastal areas (Bezuidenhout, 2020; Feng et al., 2010; Thereska, 2009). Among the different methodologies applied in these types of studies, one of the most promising is the mapping of natural radioactivity using in situ gamma spectrometers, which have been applied in both beach sands and submerged coastal areas (Androulakaki et al., 2015; Kilel et al., 2022; Tsabaris et al., 2023b). These detectors with continuous acquisition gamma spectra capability enable a rapid mapping of natural radionuclides of the study region to identify high activity concentration areas as sediment accumulation zones (Mtshawu et al., 2023; Tsabaris et al., 2023a).

Despite the advantages that in situ measurements can present (e.g., the velocity at which results can be obtained), there are still some disadvantages that need to be addressed. For example, when using in situ gamma spectrometers, interferences of the surrounding elements of the study region can alter the resulting map and some sediment transport patterns can be misinterpreted. Considering this, lab-based measurements can ensure that the activity concentration values obtained come only from the sediment grains. This is because samples are taken from the study region and analysed in the laboratory so no interference from the surrounding objects such as rocks, construction materials or seawater can occur. In addition, since these measurements come directly from the samples, lab-based measurements can also be used to enhance the knowledge of the relationships between activity concentration values and different sediment characteristics. This can lead to a better understanding of the role and application of natural radionuclides as tracers of coastal erosion, transport and accumulation of sediments.

When assessing the use of natural radionuclides as tracers of sediment dynamics, one of the key steps is to identify their spatial distribution in the study region and to determine how they are related to different sediment characteristics. In this framework, some works have found that there is an existing relationship between the activity concentrations of both natural and artificial radionuclides in sediment samples and some sedimentological variables, such as the grain size or organic content (Alfonso et al., 2014; Charkin et al., 2022; Huang et al., 2013; Ligero et al., 2001; Lin et al., 2020; Madruga et al., 2014). According to these studies, an increase in the small-grain-size fraction in sediments is associated with an increase in the activity concentration values of different radionuclides, including, for example, ^{40}K, ^{137}Cs and various radium isotopes. These studies explain that this occurs because smaller particles of sediment present larger active surfaces, which favours the sorption of radionuclides. Nevertheless, some authors found that in some circumstances, such as when the clay and/or silt fractions in the samples are low, this relationship between small grain sizes and high activity concentrations of radionuclides does not necessarily occur (Charkin et al., 2022). Thus, it cannot be assumed that high activity concentration values of natural radionuclides are always associated with the accumulation of small grain-size sediments. Therefore, further studies on the subject are necessary to enhance the knowledge of how natural radionuclides relate to sediment characteristics so their role as tracers of the sediment erosion, transport and accumulation of these sediments can be better evaluated. Understanding this is especially important to properly apply and develop emerging methodologies used in the application of natural radionuclides as tracers of sediment dynamic processes such as the in situ mapping mentioned before.

In the case of El Confital Bay, in the northern part of Gran Canaria Island (Spain), previous baseline studies on natural radionuclides and their use as tracers of sediment dynamics have focused on Las Canteras Beach, which is located in the southern part of the bay (Arnedo et al., 2013; Arriola-Velásquez et al., 2019, 2021). This beach was chosen as a natural laboratory to assess the use of natural radionuclides as tracers of sediment dynamics due to its diverse sediment dynamics and heterogeneous sediment composition. According to the literature, this beach is divided into three arches, and its northern and central arches are protected from wave action by a natural offshore rocky bar. This bar has openings and fragmentations that present themselves more in the central arch. The beach exhibits more terrigenous materials and heavy minerals in the southern arch and more calcareous and organic content in the northern arch (Alonso, 1993; Alonso and Pérez Torrado, 1992). In addition, it presents seasonal variability in its sedimentary budget. During erosion periods, the sediments from the southern arch are eroded and longshore transport to the northern arch occurs. During accumulation periods, sediments arrive at the beach from the surrounding area, and in the northern arch, some longshore transport to the southern part of the beach can occur. Thus, the northern arch has a constant accumulation period, while the southern arch presents strong differences in its sediment budget between erosion and accumulation periods (Alonso, 2005, 1993; Alonso and Vilas, 1996).

The first studies carried out in this area addressed the spatial distribution of natural radionuclides in intertidal sand from Las Canteras Beach (Arnedo et al., 2013; Arriola-Velásquez et al., 2019). The results obtained showed that the samples with lower activity concentration values were from the southern part of the beach, which is the area that is completely exposed to wave action. The samples located in front of the openings of the bar, mostly in the central arch, presented intermediate activity concentration levels. The northern arch, the area fully protected from wave action, presented the highest activity concentration values. This distribution of natural radionuclides seemed to be identifying the distribution of sediments along the beach according to the different dynamics present in it. In addition, in the work of Arriola-Velásquez et al. (2019), a first approach for determining the relationships between the activity concentration values and the sedimentological variables of the samples was assessed. The results showed that the mean grain size of the samples had a direct correlation with the activity concentration values of ^{226}Ra, ^{232}Th and ^{40}K. This indicated that samples with a larger grain size corresponded to higher activity concentration values. Furthermore, the bulk density of the samples presented an inverse correlation with the activity concentration values of those same radionuclides. Therefore, it seemed that the spatial variability of natural radionuclides also indicated the different mineral compositions of the sediments.

The study of Arriola-Velásquez et al. (2021) focused on assessing the temporal variability of the activity concentration values of natural radionuclides in sand samples during a three-year period. In this case, the influence of meteorological and oceanographic variables on the activity concentrations of ^{226}Ra, ^{228}Ra and ^{40}K was studied. The results showed the presence of significant differences that depended on the significant wave height (H_S) in the activity concentration values of these radionuclides in the southern arch of the beach. Hence, campaigns that took place in periods with a low H_S presented higher activity concentration values of ^{226}Ra, ^{228}Ra and ^{40}K. In addition, a mineralogical analysis showed that the increases and decreases in the activity concentration values agreed with the presence or absence of feldspars in the sand samples during erosion and accumulation periods.

These earlier studies seem to validate the use of natural radionuclides as tracers of the erosion, transport and accumulation of sediments in the intertidal zone of beach areas. Therefore, this study aims to use the spatial distributions of the activity concentrations of ^{226}Ra, ^{228}Ra, ^{40}K and unsupported ^{210}Pb ($^{210}Pb_{ex}$) in two periods in time to trace different sediment dynamics in submerged areas from El Confital Bay and Las Canteras Beach. Moreover, the influence of the grain size and mineralogical composition of the samples on the activity concentration values found for these radionuclides will be assessed. This way, this study will provide a methodology that could be applied in other parts of the world to study coastal sediment dynamics using natural radionuclides as tracers and can help the development of emerging methodologies in the field.

2. Study region

El Confital Bay is a 10-km^2 bay located in the northern part of the island of Gran Canaria in the city of Las Palmas de Gran Canaria, Spain (Fig. 1). According to prior studies, the sediments that compose the sand on the bottom of El Confital Bay present different composition and granulometric characteristics. The grain size varies, with sizes that range from 0.13 to 3.66 mm (Medina et al., 2006). In addition, two main groups of materials can be found in the bay. On one hand, the sediments that are present in the north-eastern part of the bay have a high carbonate content; these sediments are mostly of organic origin. On the other hand, the south-western part of the bay presents more terrigenous sediments, including sediments that come from phonolitic lava flows and basic rocks and have a low organic material content (Balcells et al., 1990; Mangas and Julià-Miralles, 2015; Medina et al., 2006; Schmincke, 1993).

The sediments of Las Canteras Beach have similar grain sizes, which range between 0.2 and 0.5 mm; slightly larger sizes are present in the area between the central and northern arches (Alonso, 1993; Arriola-Velásquez et al., 2019; Medina et al., 2006). The origin of these sediments is the geological environment of the beach, including basic rocks from the islet in the north-eastern part of the bay, the natural offshore calcarenite rocky bar, magnetite and volcanic rocks from La Ballena Ravine in the southern part of the beach and the different sediments that can be found in the submerged sandbars of El Confital Bay (Balcells et al., 1990; Schmincke, 1993). Moreover, some calcimetry and petrological analyses that have been carried out over the years allow the differentiation of the various materials that can be found at Las Canteras Beach. In the northern arch, the sand is principally composed of bioclast and calcareous materials. Hence, some studies suggested that the sediments of the northern part of the beach come from the north-eastern part of El Confital Bay through the openings of the bar in that area (Medina et al., 2006). Nonetheless, the sand from the northern arch also presents calcarenites, with a significant feldspar content in its terrigenous part (Alonso, 1993; Alonso and Pérez Torrado, 1992). In the southern arch, sediments have lower carbonate and bioclast contents. The materials that accumulate mostly come from the outlet of the ravine that ends at this arch. These materials are mostly clinopyroxenes, amphiboles, Fe-Ti oxides and other heavy minerals, such as olivine. The lighter lithics that arrive at this part of the beach also include, among other things, feldspars, but these are redistributed along the beach (Alonso, 1993; Alonso and Pérez Torrado, 1992; Mangas and Julià-Miralles, 2015; Medina et al., 2006).

3. Materials and methods

3.1. Sand sample collection and preparation

An extensive campaign was designed to evaluate the spatial distributions of the activity concentration values of various natural radionuclides for the whole study region. A total of 39 submerged sand-sampling locations were selected to cover the whole area of El Confital Bay and the submerged part of the beach located between the natural offshore rocky bar and the beachline, as well as the northern and southern arches of Las Canteras Beach, during the first half of 2022 (Fig. 1B). To better specify their locations, the samples from outside the natural offshore rocky bar were considered deep sediment samples (D). The samples from the submerged part of the beach were identified as submerged sand samples (S). Finally, the samples from the intertidal beach were called intertidal sand samples (I). In total 16 deep samples were collected in the outer part of El Confital Bay. In addition, 15 samples were collected along the submerged part of Las Canteras Beach and its entrance in the southern arch. All submerged samples were collected aboard a vessel using a 2L Van Veen grab. The sediments collected correspond to seabed surface sediments. Pictures of the sampling device used for submarine sample collection can be checked in the supplementary material (Supplementary Fig. S1). Moreover, 8 sand samples were taken in the intertidal zone of the beach during low tide. For this, a 1-m^2 square was drawn in the sand and, after mixing in situ, superficial sand samples were taken from between depths of 0 and 5 cm. In addition to these samples, 37 samples from a campaign carried out between 2005 and 2006 as part of a prior sedimentary study of El Confital Bay (Medina et al., 2006) were also analysed in this work (Fig. 1A). These samples included 16 samples from the bay, 7 from the submerged part of the beach and 14 belonging to the intertidal zone.

All sand samples were taken to the laboratory, dried at 80 °C for 24 h and sieved through a 1-mm mesh to homogenise them. Finally, they were stored in PVC-trunk conical containers, which were filled to 40 cm^3 and sealed with aluminium strips for one month before measurements were taken. This month of storage allowed the secular equilibrium between ^{226}Ra, ^{222}Rn and its short-lived progenies to be reached since ^{214}Pb is used to determine ^{226}Ra (Bezuidenhout, 2013).

3.2. Gamma spectrometry analysis

The determination of radionuclides in sand samples using gamma spectrometry analysis was carried out using a Canberra Extended Range (XtRa) Germanium spectrometer, model GX3518, with a relative efficiency of 38 % with respect to a 3″ x 3″ active area NaI (Tl) detector and a nominal FWHM of 0.875 keV at 122 keV and 1.8 keV at 1.33 MeV. It was coupled to a Canberra DSA-1000 multichannel analyser with the software package Genie 2000. The efficiency calibration of the system was carried out using the Canberra LabSOCS package based on the Monte Carlo method (Arnedo et al., 2017; Arriola-Velásquez et al., 2019, 2021; Guerra et al., 2015, 2017). The reference standards IAEA RGK-1 (potassium sulphate), RGU-1 (uranium ore) and RGTh-1 (thorium ore) were used to verify the calibration. Energy calibration was performed using ^{155}Eu/^{22}Na (Canberra ISOXSRCE, 7F06-9/10138 series) and verified using the 1460.8 keV line of ^{40}K (IAEA RGK-1) (Arnedo et al., 2017).

Different photopeaks were analysed to determine the radionuclides of interest. The emission line 351.9 keV of ^{214}Pb was used to determine the activity concentration of ^{226}Ra. ^{210}Pb was directly measured using the emission line of 46.5 keV. The emission line of 911.2 keV, corresponding to ^{228}Ac, was used to obtain the activity concentration values of ^{228}Ra. The lines 1460.8 keV and 661.8 keV were used to directly measure the activity concentrations of ^{40}K and ^{137}Cs, respectively. The counting time for each sample was around 24 h. The activity concentration values have been expressed according to common standard of using only one significative figure for uncertainties, and a coverage factor k = 1 was assumed.

Moreover, the unsupported or excess ^{210}Pb (^{210}Pb$_{ex}$) was calculated from the activity concentrations of ^{210}Pb and ^{226}Ra. ^{222}Rn has a half-life of 3.8 days, and its decay produces ^{210}Pb. ^{222}Rn is a gas daughter of ^{226}Ra that partially diffuses into the atmosphere, where it rapidly decays into ^{210}Pb. After this, ^{210}Pb falls back to the Earth's surface through wet and dry deposition. This deposited ^{210}Pb that is not in equilibrium with the ^{226}Ra of the samples is what is known as unsupported or excess ^{210}Pb$_{ex}$ (Bobos et al., 2021; Dueñas et al., 2017; Gaspar et al., 2017; Gu et al., 2022; Hülse and Bentley, 2012). Therefore, the difference between the activity concentrations of ^{210}Pb and ^{226}Ra was used to determine the activity concentration of ^{210}Pb$_{ex}$.

3.3. Grain size and X-ray diffraction analysis

A dry-sieving grain size analysis (Alveirinho Dias, 2004) was performed on the samples from El Confital Bay and Las Canteras Beach. Aliquots of around 300 g of each sample were used. These aliquots were passed through nine sieves from 8 to 0.0625 mm with 1φ intervals, and each portion was weighed separately. After, the results of the granulometric analysis including the statistical parameters of mean grain size, sorting (standard deviation), skewness and kurtosis and the percentage of the different grain size fractions were obtained from the GRADISTAT

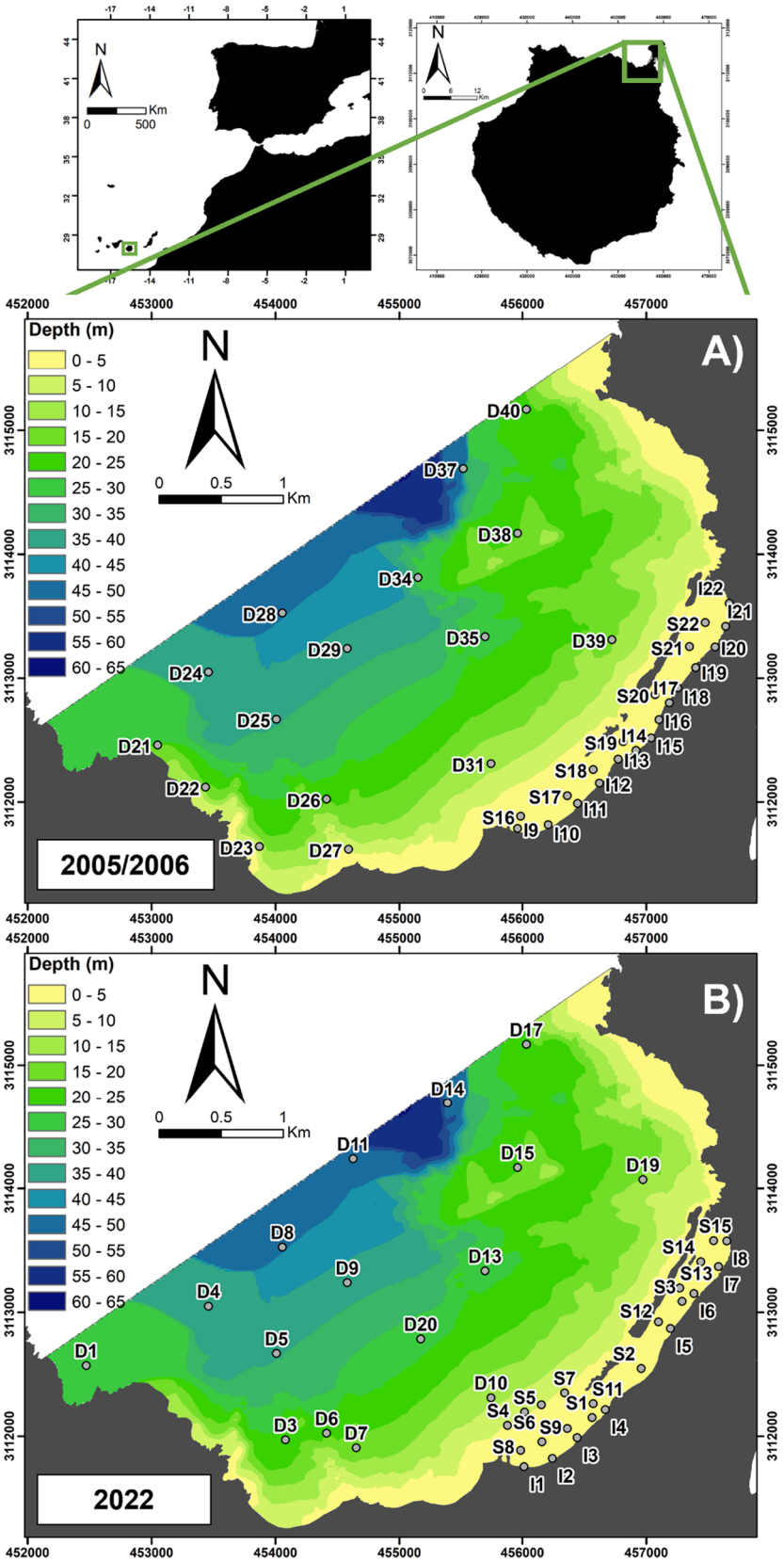

Fig. 1. Study region, bathymetry and sand sampling points in El Confital bay and Las Canteras beach for the 2005/2006 and the 2022 campaigns. Coordinates are in the UTM system.

software version 9.1 (Blott and Pye, 2001) using the Folk and Ward method (Folk and Ward, 1957). Then, each grain size fraction of the sand was stored in PVC-trunk conical containers, just like the original samples, for gamma spectrometry analysis.

Powder X-ray diffraction (XRPD) data acquisition was carried out with an X'Pert PRO Diffractometer (PANalytical), using the θ-2θ Bragg-Brentano geometry, that was equipped with an X'Celerator LPS detector. The 5°-80° 2θ range was investigated using CuKα radiation with a current tension of 40 kV, a current intensity of 40 mA and collection at 0.02° steps, and a fixed divergence-slits angle of 0.25°. Samples were ground on an agate mortar and then pressed in a back-load sample holder. The sample holder was spun during data acquisition. Diffraction patterns were analysed using X'Pert HighScore v. 2.1 (PANalytical©) and mineral phases were matched using PDF2 (ICDD). Quantitative analysis through Rietveld refinement was carried out using GSAS II (Toby and von Dreele, 2013) and crystallographic information files (CIFs) available in the literature and obtained from the Crystallographic Open Database – COD (Gražulis et al., 2009) for closely related matched phases. No clear evidence of amorphous material was observed on the pattern of diffraction ruling out a significant contribution of glassy material.

Selected grains of sample S8 were also checked using single crystal X-ray diffraction (SCXRD) using a Rigaku Oxford Diffraction XtaLAB Synergy diffractometer equipped with a PhotonJet (Mo) X-ray Source operating at 50 kV and 1 mA, and a Hybrid Pixel Array detector that was located 62 mm away from the sample position. Intensity data were extracted from images using CrysAlisPro 1.171.40.71a (Rigaku Oxford Diffraction, 2020). Crystal structures were refined using SHELX-2018 (Sheldrick, 2015), starting with atom coordinates from the literature. Crystallographic information files have been provided as supplementary material.

3.4. Map interpolation method

The maps of bathymetry, grain size and activity concentration values of ^{226}Ra, ^{228}Ra, ^{40}K and ^{210}Pb$_{ex}$ were drawn using the ArcGIS Desktop version 10.8.2. The interpolation algorithm used in all cases was the Inverse Distance Weighted (IDW). For IDW, it was used the formula that takes the inverse of the distance raised to the second power, which is the default in the ArcGIS and it is the most simple and widely used (Achilleos, 2011; Gong et al., 2014).

3.5. Statistical analysis

On the one hand, to establish the possible significant differences among the measurements of the activity concentration values from both campaigns, a u-test (IAEA, 2012) was performed using the following equation:

$$u_{test} = \frac{|A_A - A_B|}{\sqrt{u_A^2 + u_B^2}} \quad (1)$$

where A_A corresponds to the mean activity concentration value of one radionuclide in the campaign of 2005/2006, u_A is the uncertainty associated with that mean activity value, A_B is the mean activity concentration value of one radionuclide in the campaign of 2022 and u_B is the uncertainty of that activity concentration value. The u_{test} values obtained from Eq. (1) are compared with the threshold value 2.58 at level 99 %. Then, the null hypotheses of equality of activity concentration values are rejected for observed u_{test} values greater than 2.58. Therefore, when $u_{test} > 2.58$, the pair of values reported is significantly different.

On the other hand, a Shapiro-Wilk normality test (Shapiro and Wilk, 1965) was used to evaluate the distribution of all the results. Then, a correlation analysis was performed to establish the relationships between the activity concentration values of ^{226}Ra, ^{228}Ra, ^{40}K and ^{210}Pb$_{ex}$, the results of the granulometric analysis and the depth and bulk density values of the samples. In the case of the grain size fractions, if the activity concentrations of one radionuclide followed a normal distribution, a one-way ANOVA test was performed to determine if there were significant differences among the different grain size fractions. Then, Tukey's Honestly Significant Difference (HSD) test (Williams and Abdi, 2010) was used to establish the exact fractions within which significant differences were found. If the activity concentrations did not follow a normal distribution, a Kruskal-Wallis test (Theodorsson-Norheim, 1986) was used to determine if there were significant differences in the activity concentrations of samples with different grain sizes. In this case, a Wilcoxon rank-sum test (Rosner and Glynn, 2009) was applied to determine which grain size fractions presented such differences. These tests were carried out for a significance level of 0.05.

4. Results and discussion

4.1. Activity concentration distribution in sediment samples from El Confital Bay and Las Canteras Beach

The maps in Fig. 2 show the superficial sediment mean-grain-size distribution in El Confital Bay and Las Canteras Beach in both campaigns, 2005/2006 and 2022. Both maps show that most of the sediment with a higher mean grain size can be found in the south-western and north-eastern parts of the bay. In the case of the campaign of 2005/2006, the largest mean grain size was 2432 μm with sorting of 1.589, skewness of −0.140 and kurtosis of 1.188, while in the 2022 campaign, the maximum mean grain size was 1617 μm with sorting of 1.617, skewness of 0.087 and kurtosis of 1.354. However, the average grain size for all the samples of the bay in the 2005/2006 campaign was 473 μm (0.473 mm), while for 2022, it was 379 μm (0.379 mm). This means that, in both cases, the mean grain size of the whole bay classifies the sediments as medium sand according to the GRADISTAT software classification (Blott and Pye, 2001).

The activity concentration distributions of ^{226}Ra, ^{228}Ra and ^{40}K for the whole bay for both campaigns are represented in Fig. 3. The maximum, minimum and mean activity concentration values of these radionuclides are reported in Table 1. The mean activity concentration values of ^{226}Ra, ^{228}Ra and ^{40}K in both campaigns were compared using the u-test, and the results are also displayed in Table 1. The results of the test show that the mean values do not present significant differences between the campaigns. This suggests that in essence, the activity concentration values of ^{226}Ra, ^{228}Ra and ^{40}K correspond to the same sediments in both periods. From the maps in Fig. 3, it can be observed that the activity concentrations of ^{226}Ra, ^{228}Ra and ^{40}K have the same main spatial distribution in both campaigns, which can be used to delimit two areas: one with lower activity concentration values in the north-eastern part of the bay and one with higher activity concentration values in the south-western part of the bay.

Earlier studies of environmental radioactivity in volcanic islands showed that phonolitic rocks are among the volcanic rocks that present higher natural gamma radiation emissions and activity concentration values of ^{226}Ra, ^{232}Th (parent radionuclide of ^{228}Ra) and ^{40}K (Arnedo et al., 2017; Chiozzi et al., 2001; Fernández-Aldecoa et al., 1992). In fact, the work of Arnedo et al., (2017) reported that soils from the island of Gran Canaria in which phonolitic and trachytic rocks could be found presented the highest activity concentration values of ^{226}Ra (>50 Bq kg^{-1}), ^{232}Th (>90 Bq kg^{-1}) and ^{40}K (>1000 Bq kg^{-1}). As a matter of fact, the mean activity concentration values reported in the study of Arnedo et al., (2017) for this type of soil for ^{226}Ra and ^{40}K (75 Bq kg^{-1} and 869 Bq kg^{-1} respectively) clearly contrast with the mean activity concentration values reported for soils of basaltic rocks (30 Bq kg^{-1} for ^{226}Ra and 337 Bq kg^{-1} for ^{40}K). Therefore, the high activity concentration values obtained for the south-western part of the bay seem to be related to the presence of sediments from phonolitic rocks in the area (Balcells et al., 1990; Schmincke, 1993). On the other hand, in the case of the

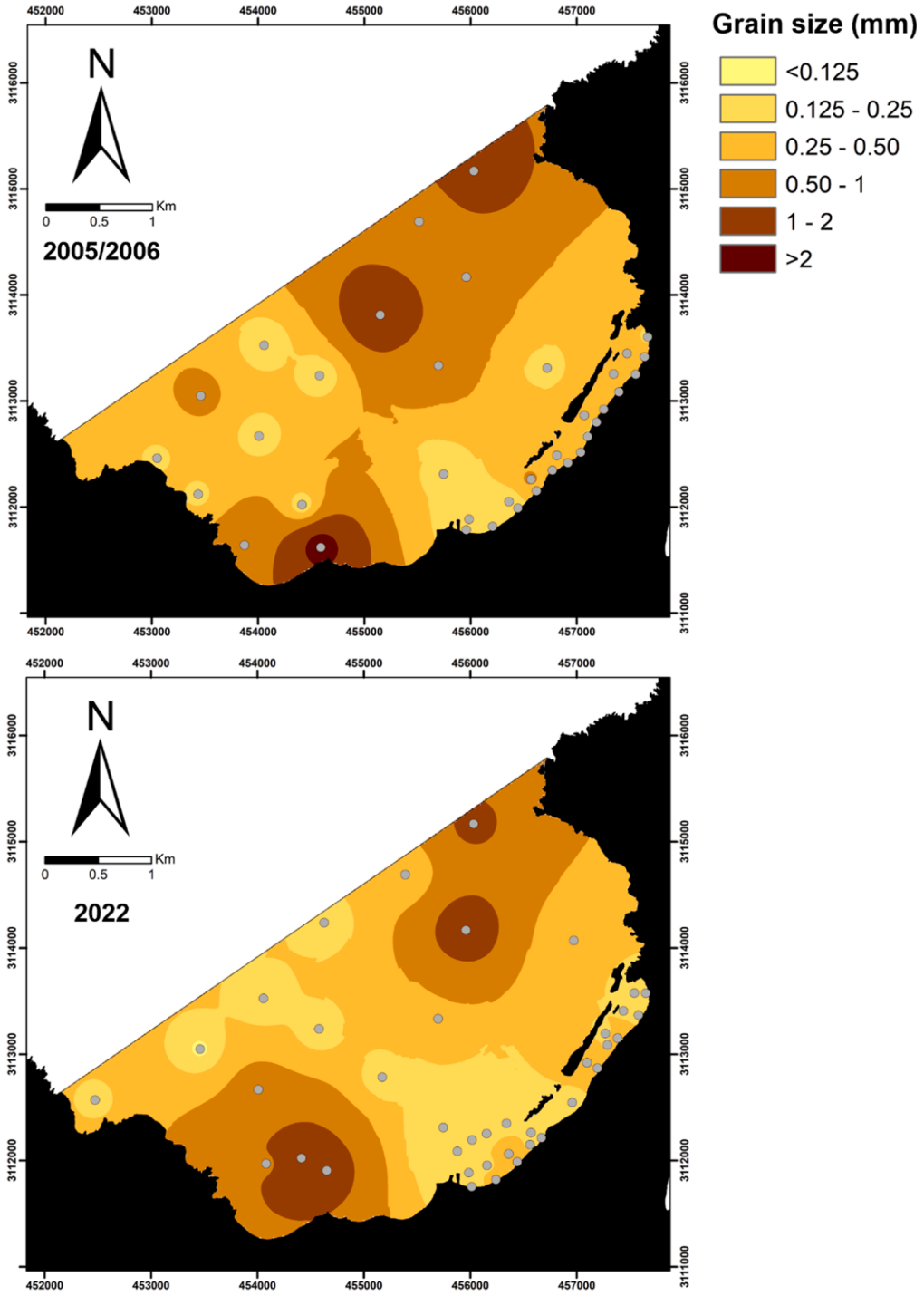

Fig. 2. Sediment grain size distribution of El Confital bay and Las Canteras beach for the 2005/2006 and the 2022 campaigns.

north-eastern part of the bay, preceding descriptions of El Confital Bay established a predominant content of CaCO3 in sediments from that area with values of more than 90 % of $CaCO_3$ content (Medina et al., 2006). This clearly indicates that the sediments from the north-eastern part of the bay have a predominant composition of bioclasts. Some studies in other parts of the world have found that increases and decreases in ^{226}Ra, ^{232}Th and ^{40}K in sediments are related to, among other factors, the amount of organic matter that can be found in such sediments (Alfonso et al., 2014; Ramadan and Diab, 2013). For those authors, a higher organic matter content was correlated with higher activity concentration values of different radionuclides. However, in the case of El Confital Bay, the area with the highest carbonate and organic content seems to be the one with lower activity concentration values of ^{226}Ra, ^{228}Ra and ^{40}K. This discrepancy could be explained by two characteristics of the sediments in the study region considered in this work.

First, in the studies mentioned earlier, the higher activity concentration values seemed to be related to the adsorption of radionuclides in the sediments with a small grain size and a high organic content. According to these studies, this occurs due to the larger active surface of the smaller grains of such sediments. However, the map in Fig. 2 shows that the north-eastern part of El Confital Bay has larger mean grain sizes, with all the samples being classified as medium to very coarse sand by the GRADISTAT software (Blott and Pye, 2001). Therefore, it could be possible that in areas like El Confital Bay, sediments with high carbonate

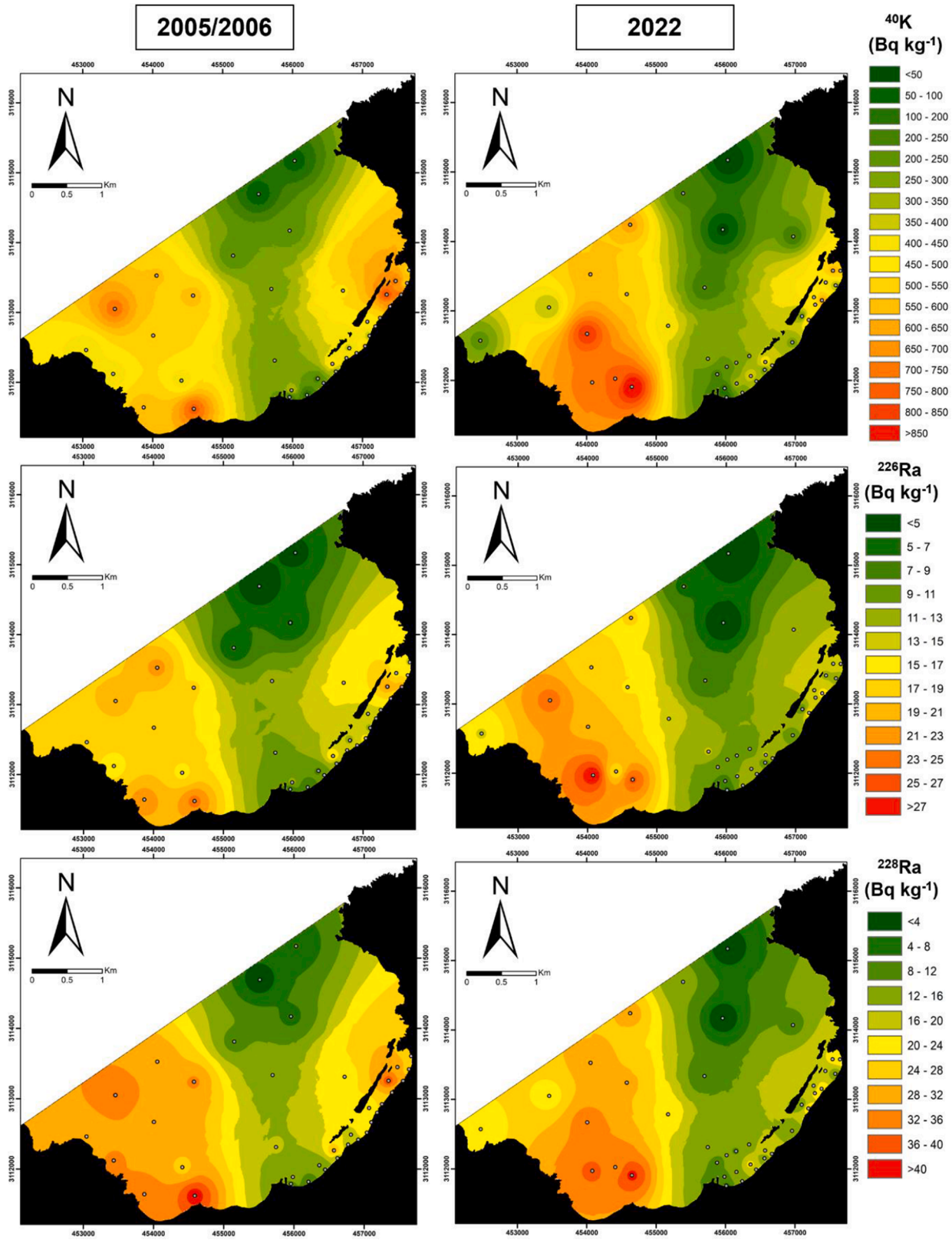

Fig. 3. Activity concentration distribution of ^{40}K, ^{226}Ra and ^{228}Ra in sediments from El Confital bay for the 2005/2006 and the 2022 campaigns.

and organic contents have larger grain sizes and correspondingly a smaller active surface. Thus, this adsorption of radionuclides might be less likely to occur.

Second, in prior studies of Las Canteras Beach, which is located in El Confital Bay and accordingly shares its geological characteristics, it was proven that the part of the beach with more carbonates presented higher activity concentration values of ^{226}Ra, ^{228}Ra and ^{40}K (Arriola-Velásquez et al., 2019, 2021). However, this increase in the activity concentration values of those three radionuclides, especially ^{40}K, seemed to be more related to the accumulation of K-feldspars (minerals typically found in

Table 1
Ranges of activity concentration values of ^{226}Ra, ^{228}Ra and ^{40}K in Bq kg^{-1} in the whole study region for both campaigns (2005/2006 and 2022). The mean activity concentration value for each radionuclide in each campaign is also reported in parenthesis below each range. In addition, the result of the u-test described in IAEA, (2012) is given.

Campaign	^{226}Ra	^{228}Ra	^{40}K
2005/ 2006	2.9 ± 0.7 – 24 ± 1 (13.8 ± 0.9)	< MDA (2) – 42 ± 3 (22 ± 2)	68 ± 8 – 820 ± 40 (420 ± 20)
2022	< MDA (1) – 29 ± 1 (13.1 ± 1.0)	< MDA (2) – 41 ± 3 (18 ± 2)	< MDA (3) – 940 ± 40 (380 ± 20)
u_{test}	0.54	1.27	1.37

(1) Minimum detectable activity (MDA) for ^{226}Ra = 2.9 Bq kg^{-1}

(2) MDA for ^{228}Ra = 2.8 Bq kg^{-1}

(3) MDA for ^{40}K = 29 Bq kg^{-1}

phonolitic rocks) in the areas with high carbonate and organic matter contents. Furthermore, earlier studies also indicated that feldspars could be found in the part of the beach with a higher carbonate content due to the presence of calcarenites, which contain feldspar in their terrigenous component (Alonso, 1993; Alonso and Pérez Torrado, 1992). Hence, the higher activity concentration values of ^{226}Ra, ^{228}Ra and ^{40}K found in sediments in the studies of 2019 and 2021 were apparently more related to the terrigenous content of the sediments than to the physico-chemical interactions of the carbonates and organic matter with the natural radionuclides of the environment. As mentioned earlier, a prior study showed that the north-eastern part of the beach possessed higher carbonate and foraminifera contents and less terrigenous content in its sediments (Medina et al., 2006). This, therefore, suggests another reason that the activity concentration values found for ^{226}Ra, ^{228}Ra and ^{40}K in that area are lower. Considering all of this, and since the north-eastern part of the bay has a lower terrigenous content and a larger grain size, the low activity concentration values found for this area in this work are to be expected. Nevertheless, the results of a mineralogical analysis of samples from different parts of the bay will be discussed later in this work to further understand the influence of these factors on the activity concentration values of the samples.

When comparing the spatial distributions of the activity concentration values of ^{226}Ra, ^{228}Ra and ^{40}K for both campaigns (Fig. 3), some differences can be observed. The lack of significant differences between the mean activity concentration values of the campaigns suggests that these distinctions could be associated with sediment transport within the study region. Focusing on the south-western part of the bay, the area with the highest activity concentration values seems to have moved from the edge of the bay to its interior. Furthermore, by comparing the two maps of the grain size distribution shown in Fig. 2, it can also be observed that in that same part of the bay, the larger-grain-size sediments also seem to have shifted in the same direction as the area with the highest activity concentration values of ^{226}Ra, ^{228}Ra and particularly ^{40}K. Given that high activity concentration values identify the accumulation of sediments and considering that the same shift patterns appear for the grain size distribution and activity concentration maps, this may suggest that there is some transport and accumulation of sediments from the coastline into the interior of the bay. To find possible agents controlling this sediment transport, the depth of closure (d1) was calculated for every year from 2005 to 2021. The depth of closure can be described as the limiting water depth at which there is no cross-shore sediment transport (Hallermeier, 1981). It was calculated using the following equation:

$$d_1 = 2.28H_{12h/y} - 68.5\left(\frac{H^2_{\frac{12h}{y}}}{gT^2_{\frac{12y}{y}}}\right) \quad (2)$$

where $H_{12h/y}$ corresponds to the highest significant wave height that is exceeded 12 h a year, $T_{12h/y}$ corresponds to the period associated with this height and g is the gravitational acceleration. The data of the significant wave height and the period associated to it were obtained from a buoy of the Puertos del Estado surveillance network, belonging to the government of Spain. The results obtained are shown in Table 2 and indicate that for almost every year, the depth of closure is located at less than 10 m, with a mean value of 8.6 m with a standard deviation of 1.3 m. However, in 2014, the significant wave height was higher than in other years, allowing the closure depth to descend to 12 m. Hence, it seems that in El Confital Bay, sand located at greater depths than 10 m could also be transported by the wave action during strong storm events. This could explain the sediment transport that Fig. 3 suggests for the south-western part of the bay. Nevertheless, further analysis on the coastline evolution of the area should be necessary to confirm the sediment transport that the changes in the activity concentration of ^{226}Ra, ^{228}Ra and ^{40}K suggest and the causes behind it.

Since the depth of closure established that the area where the net exchange of sediment can occur is at less than 10 m depth, the activity concentration distributions of ^{226}Ra, ^{228}Ra and ^{40}K for both campaigns are represented in more detail for the submerged and intertidal parts of Las Canteras Beach in Fig. 4. In both cases, the three radionuclides show higher activity concentration values in the submerged and intertidal parts of the northern arch of the beach and lower activity concentration values in the southern arch. The results agree with what was found in previous studies of the intertidal zone of this beach (Arriola-Velásquez et al., 2019, 2021). Those works ascertained that for the intertidal zone of Las Canteras Beach, the protected part of the beach experienced a constant accumulation of sediments, and thus, this was the part that presented higher activity concentration values of ^{226}Ra, ^{228}Ra and ^{40}K. On the other hand, the southern arch of the beach (the area that was totally exposed to wave action) was identified as an erosion area, and the activity concentration values of the radionuclides in this area were lower. Taking this into consideration, the results displayed in Fig. 4 also identify the accumulation area in the submerged northern arch, where activity concentration values are higher. However, the lower activity concentration values of ^{226}Ra, ^{228}Ra and ^{40}K in the submerged southern arch establish it as an erosion area. In addition, Fig. 4 displays a

Table 2
Significant wave height that is exceeded 12 h a year ($H_{12h/y}$), associated period ($T_{12h/y}$) and depth of closure (d1) for every year since 2005 to 2021.

Year	$H_{12h/y}$ m	$T_{12h/y}$ s	d1 m
2005	3.6	16.4	7.9
2006	3.7	12.7	7.8
2007	3.6	18.1	8.0
2008	4.4	17.9	9.6
2009	4.2	15.6	9.1
2010	3.9	17.3	8.6
2011	3.7	17.9	8.0
2012	3.1	16.6	6.7
2013	3.5	17.5	7.7
2014	5.9	13.6	12.1
2015	4.0	11.2	8.1
2016	4.0	16.2	8.6
2017	3.5	13.6	7.6
2018	4.4	19.5	9.6
2019	4.8	16.1	10.4
2020	4.3	16.1	9.2
2021	3.8	10.0	7.6

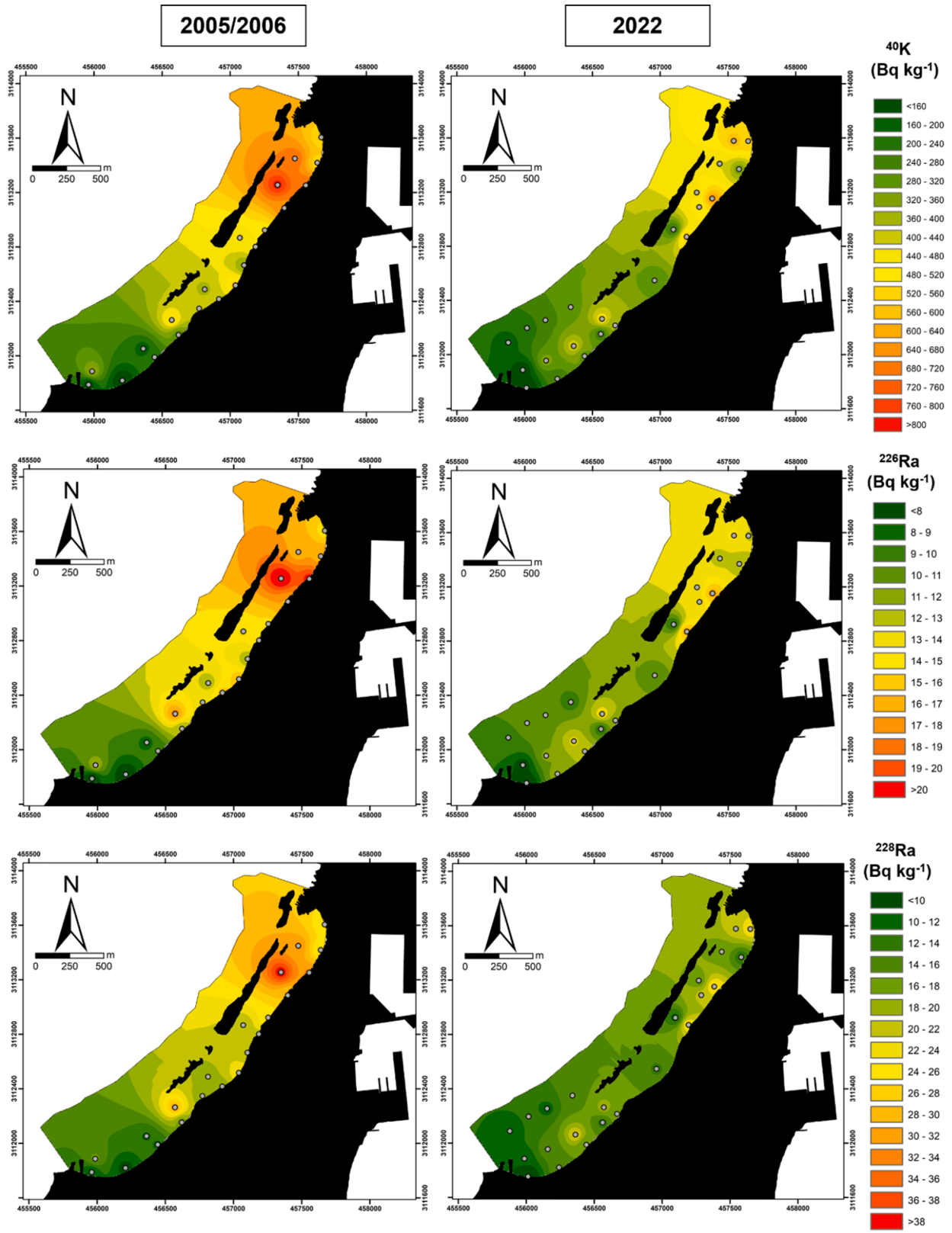

Fig. 4. Activity concentration distribution for ^{40}K, ^{226}Ra, and ^{228}Ra in sediments from Las Canteras beach for the 2005/2006 and the 2022 campaigns.

progressive increase in the activity concentration values of these three radionuclides from the southern arch to the northern arch. This also agrees with what was found in earlier works on the area (Arriola-Velásquez et al., 2019, 2021) and depicts, in both cases, for the intertidal and submarine parts of the beach, the longshore marine transport of sediments, which, according to the literature, occurs from the southern arch to the northern arch (Alonso, 1993; Alonso and Vilas, 1996).

Focusing on the accumulation area of the beach (the submerged and intertidal northern arch), the mean activity concentration value of ^{226}Ra in the 2005/2006 campaign was 17 ± 1 Bq kg^{-1}, and in the 2022

campaign, it was 13.4 ± 1.0 Bq kg^{-1}. For ^{228}Ra, the mean activity concentration values of the 2005/2006 and 2022 campaigns were 29 ± 2 and 19 ± 2 Bq kg^{-1}, respectively. Finally, ^{40}K presented a mean activity concentration value of 640 ± 30 Bq kg^{-1} for the 2005/2006 campaign and 470 ± 20 Bq kg^{-1} for the 2022 campaign. When comparing both campaigns, it can be seen that the mean activity concentration values of ^{226}Ra, ^{228}Ra and ^{40}K are higher in the 2005/2006 campaign, with differences of 4 ± 1 Bq kg^{-1} for ^{226}Ra, 10 ± 3 Bq kg^{-1} for ^{228}Ra and 170 ± 40 Bq kg^{-1} for ^{40}K. In the work of Arriola-Velásquez et al., (2019, 2021), it was suggested that even though the protected part of the intertidal beach is experiencing the constant accumulation of sediments, the intensity of the accumulation varied between months. Such changes in the intensity of accumulation were identified by monthly variations in the activity concentration values of ^{226}Ra, ^{228}Ra and ^{40}K during the three-year period of that study (Arriola-Velásquez et al., 2021). In that work, the mean activity concentration values for the samples belonging to the intertidal accumulation area (described as zone III) were calculated for each month. The results showed that the minimum and maximum activity concentration values of ^{226}Ra for that area were 13.6 ± 0.9 and 20 ± 1 Bq kg^{-1}, respectively. In the case of ^{228}Ra, the minimum activity concentration value was 16 ± 2 Bq kg^{-1} and the maximum activity concentration value was 29 ± 2 Bq kg^{-1}. In the case of ^{40}K, the minimum activity concentration value was 500 ± 20 Bq kg^{-1} and the maximum activity concentration value was 740 ± 30 Bq kg^{-1} (Arriola-Velásquez et al., 2021). This means that according to this previous study, the differences between the minimum and maximum activity concentration values in the accumulation area were 6 ± 1 Bq kg^{-1} for ^{226}Ra, 13 ± 3 Bq kg^{-1} for ^{228}Ra and 240 ± 40 Bq kg^{-1} for ^{40}K. Considering all of this, the differences in the mean activity concentration values of ^{226}Ra, ^{228}Ra and ^{40}K found in this study are within the maximum differences that were found in the 2021 study. Therefore, it seems that the differences that can be found in this work between the activity concentration values of ^{226}Ra, ^{228}Ra and ^{40}K for both campaigns in the submerged and intertidal zones of Las Canteras Beach could be related to the monthly oscillations found in 2021. Hence, the samples from the campaign of 2005/2006 were most likely collected during a period with a more intense accumulation of sediments compared to the 2022 samples.

In Fig. 5, the activity concentration distribution of ^{210}Pb$_{ex}$ for all of El Confital Bay (Fig. 5A) during the 2022 campaign is shown, and a more detailed image of its activity concentration distribution for the intertidal and submerged parts of Las Canteras Beach (Fig. 5B) during the 2022 campaign is also given. The samples from the 2005/2006 campaign were measured approximately 12 years after collection, and a radioactive decay correction was applied to them due to the half-life of ^{210}Pb (22 years). However, due to the amount of time that had passed between sampling and measurement, the results after the decay correction were unreliable. Thus, it was decided to only analyse the 2022 data since they did not require such a radioactive decay correction. In addition, the colour scale of Fig. 5B was modified to avoid confusion with the colour scale of Fig. 5A when both images are being interpreted.

Unsupported ^{210}Pb (^{210}Pb$_{ex}$) has a mainly atmospheric origin; it travels in the lower atmosphere adsorbed to small particles that reach the planet surface through wet or dry deposition (Dueñas et al., 2017; Gaspar et al., 2017). For the Canary Islands, it has been reported that one of the main inputs of natural radionuclides is the African aeolian dust depositions (López-Pérez et al., 2020), which are also known to be carriers of ^{210}Pb (Gordo et al., 2015). Once these aeolian dust particles arrive at the sea surface, they enter the water column and slowly sink, experiencing more scavenging of ^{210}Pb on their way to the seafloor (Hülse and Bentley, 2012). Depending on whether the erosion of the seabed is weaker or stronger, accumulation due to the sedimentation of these aerosols will be more or less favoured. Therefore, it would be expected that high ^{210}Pb$_{ex}$ activity concentration values would trace the less-eroded seabed areas where accumulation occurs.

For all of El Confital Bay, the activity concentration values of ^{210}Pb$_{ex}$ ranged from 15 ± 7 Bq kg^{-1} to 270 ± 20 Bq Kg^{-1} and had a mean value of 69 ± 9 Bq kg^{-1}. This indicates that there were large variations between different parts of the bay, which can be observed in Fig. 5A. The map shows a distribution that seems to agree with the bathymetry of the study region from Fig. 1. The higher activity concentration values of ^{210}Pb$_{ex}$ appear in the deeper areas of the bay, and lower activity concentration values appear in the shallower areas. This is because at higher depths in the water column, the reduced erosion of the seabed favours the sedimentation of the aerosol particles that carry ^{210}Pb$_{ex}$. Conversely, at shallower depths, there is more erosion of the seafloor, and thus, the sedimentation of these particles is less likely to happen. Hence, this explains why the activity concentration distribution of unsupported ^{210}Pb in El Confital Bay agrees with its bathymetry.

Fig. 5B shows the activity concentration distribution of ^{210}Pb$_{ex}$ in the submerged and intertidal zones of Las Canteras Beach. The activity concentration values ranged from 15 ± 7 Bq kg^{-1} to 86 ± 9 Bq kg^{-1} and had a mean value of 38 ± 8 Bq kg^{-1}. In Fig. 5B, the spatial distribution of ^{210}Pb$_{ex}$ delimits two areas. On the one hand, there is an area of low activity concentration values located in the open part of the beach. This area is totally exposed to wave action, and thus, there is constant erosion of the seabed, which prevents the sedimentation of the aerosol particles from occurring. Therefore, the activity concentration values of ^{210}Pb$_{ex}$ are lower in this part of the beach. On the other hand, the area of the beach that is protected from wave action by the natural offshore rocky bar presented higher activity concentration values. This is because, as mentioned before, the natural offshore rocky bar, and even the

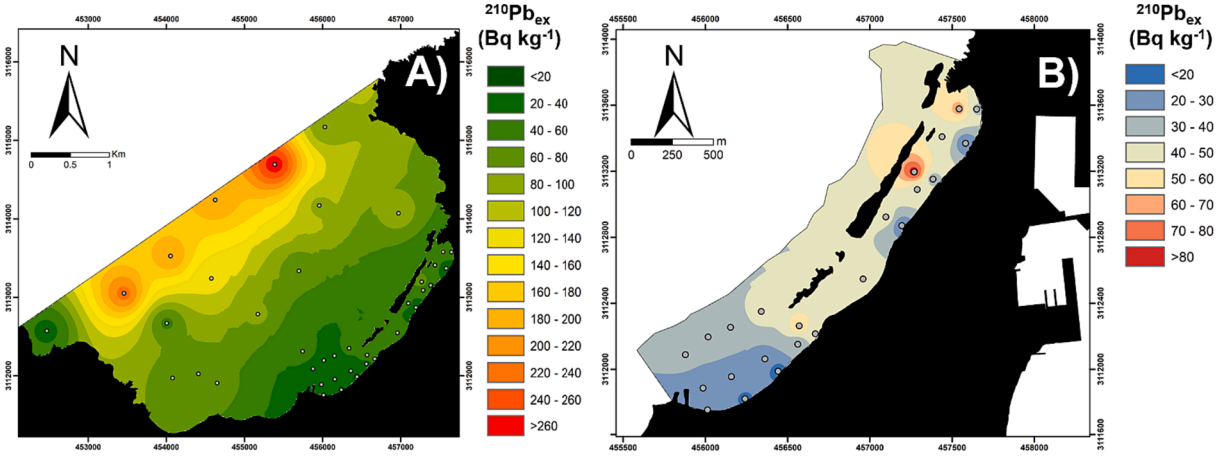

Fig. 5. Activity concentration distribution of ^{210}Pb$_{ex}$ in the 2022 campaign for A) El Confital bay and B) Las Canteras beach.

morphology of the bay, act as barriers against wave action (Alonso, 1993; Alonso and Vilas, 1996; Medina et al., 2006), generating an area with low erosion of the seafloor. Hence, the sedimentation of the particles of aeolian dust bearing $^{210}Pb_{ex}$ on the seafloor is enabled, and activity concentration values are higher in this part of the beach.

Focusing on the protected part of Las Canteras Beach, some differences can also be found in the submerged part of this beach. In the areas located near the structures of the natural offshore rocky bar, the activity concentration values of $^{210}Pb_{ex}$ are higher. This can occur because near the openings of the bar, its own structure, as well as the beach morphology, create some sheltered zones. These are calmer areas where the sedimentation of the aeolian dust carrying unsupported ^{210}Pb on the seafloor is even more favoured. Hence, higher activity concentration values of $^{210}Pb_{ex}$ appear in these areas. Considering the results obtained for both the entirety of El Confital Bay and Las Canteras Beach, it could be said that $^{210}Pb_{ex}$ can be used to identify sedimentation areas for aerosol particles on the seafloor.

4.2. Influence of the grain size on the activity concentration values of sand samples

In order to evaluate the influence of grain size in the activity concentration values of ^{226}Ra, ^{228}Ra, ^{40}K and $^{210}Pb_{ex}$ a correlation and a significant differences analysis were carried out. On one hand, a Shapiro-Wilk normality test (Shapiro and Wilk, 1965) was applied to the activity concentration values of ^{226}Ra, ^{228}Ra, ^{40}K and $^{210}Pb_{ex}$, the depth of collection, the bulk density, the mean grain size, sorting and the percentages of coarse sand, medium sand, fine sand, very fine sand and mud (clay + silt) of the samples. The percentages of larger-grain-size fractions, such as gravel and very coarse sand, were not considered because most of the samples presented a mean grain size below 1 mm and thus, the activity concentration values of the samples were only measured in sediments with a grain size below 1 mm. At a 0.05 significance level, most parameters followed a non-normal distribution. Therefore, the Spearman correlation coefficient was used to evaluate the correlations existing between the different activity concentration values and the remaining parameters. Since the mean depth of closure was established at 8.6 m, the correlation analysis was carried out for two different areas; the deeper part from El Confital Bay located below the depth of closure and the area above the depth of closure (including the submerged and intertidal zones of Las Canteras Beach).

On the other hand, 21 samples were selected from the 2022 campaign and separated into different grain size fractions that were analysed individually using gamma spectrometry to identify their activity concentrations of ^{226}Ra, ^{228}Ra, ^{40}K and $^{210}Pb_{ex}$. These samples included 6 from the high activity area of the deeper part of the bay (D3, D5, D7, D8, D9 and D11), 7 samples from the low activity area (D4, D10, D13, D14, D15, D17 and D19), 4 samples from the submerged part of Las Canteras Beach (S12, S13, S14 and S15) and 4 samples from the intertidal zone of the beach (I5, I6, I7 and I8). For a better analysis of the significant differences among grain sizes, the samples were divided into 4 categories (Table 3) following the GRADISTAT software sediment classification (Blott and Pye, 2001). The results of a Shapiro-Wilks normality test showed that at a significance level of 0.05, the activity concentration values of ^{226}Ra, ^{228}Ra and ^{40}K in the different grain size fractions followed a normal distribution, while $^{210}Pb_{ex}$ presented a non-normal distribution. Thus, a one-way ANOVA was applied to evaluate the significant differences in the activity concentrations of ^{226}Ra, ^{228}Ra and ^{40}K and a Kruskal-Wallis test was applied to $^{210}Pb_{ex}$.

Table 3
Grain size category classification. The grain size is given in mm. The number of samples obtained for each category is also indicated.

Category	Number of samples	Sediment grain size	Classification
A	13	0.5 – 2	Very coarse and coarse sand
B	16	0.25 – 0.5	Medium sand
C	16	0.125 – 0.25	Fine sand
D	9	<0.125	Very fine sands and mud

Tables 4A and 4B show the results obtained for the correlation analysis of the deeper samples from El Confital Bay and the submerged and intertidal parts of Las Canteras Beach respectively. In both analyses, ^{226}Ra, ^{228}Ra and ^{40}K were highly correlated between them. This suggests that their activity concentration values are related to the geochemical composition of the samples. Regarding the grain size fraction and the rest of the parameters, in the samples of the deeper parts of El Confital Bay, no correlation was found between them and the activity concentration values of ^{226}Ra, ^{228}Ra and ^{40}K. However, in the case of Las Canteras Beach, a direct correlation was found between the activity concentration values of these radionuclides, the grain size and the percentage of coarse sand. Moreover, in the case of the beach, an inverse correlation also appeared between the activity concentration values of these radionuclides and the percentage of very small sand and the bulk density. Thus, the results of the correlation analysis show that for the deeper parts of El Confital Bay, the activity concentration values of ^{226}Ra, ^{228}Ra and ^{40}K did not seem to be influenced by the grain size while in Las Canteras Beach higher activity concentration values of these radionuclides were found in lighter sediments with a larger grain size.

Moreover, Table 5A shows the results for significant differences of ^{226}Ra, ^{228}Ra and ^{40}K in the different grain size categories. While no significant differences were found, the boxplots from Fig. 6 show that 75 % of the samples in category A presented the highest activity concentration values of these radionuclides. This also agrees with the results of the correlation analysis indicating that, if something, higher activity concentration values of these radionuclides seem to appear in the larger grain size samples.

All these results were contrary to what other studies have found in other parts of the world, where the sediments that had higher clay and silt fractions presented higher activity concentration values due to the physico-chemical interactions of the radionuclides with the small-grain-size sediments (Alfonso et al., 2014; Ligero et al., 2001; Lin et al., 2020; Patiris et al., 2016). However, some authors have also suggested that in the absence or reduced presence of clay and silt fractions, the activity concentration values of sediments were not associated with the grain size of the sample or that the direct correlation between small grain size and high activity concentration might only be applicable in parts of the world with certain geological characteristics (Charkin et al., 2022; Ligero et al., 2001). Moreover, there are cases in which the activity concentration values of different radionuclides have been used to identify the sediment sources in areas with different lithologies, independent of the sediment grain size (Zebracki et al., 2015).

Furthermore, previous works carried out in the intertidal zone of Las Canteras Beach indicated that the higher activity concentration values of ^{226}Ra, ^{228}Ra and ^{40}K were found in samples with low density and high grain size (Arriola-Velásquez et al., 2019) and that they were also associated with an increase in K-feldspars during accumulation periods (Arriola-Velásquez et al., 2021). Considering the literature and the results from this study, it seems that the changes in activity concentration values of ^{226}Ra, ^{228}Ra and ^{40}K in the whole of El Confital Bay might be more directly related to the changes in their mineralogical composition than to grain size variations.

Regarding $^{210}Pb_{ex}$, no correlation was found with the activity concentration values of ^{226}Ra, ^{228}Ra and ^{40}K neither in the deeper part of El Confital Bay nor in Las Canteras Beach. In addition, for the deeper samples, direct correlations with the percentages of very fine sand, mud, and depth and an inverse correlation with the bulk density were reported. In the case of Las Canteras Beach, a direct correlation between the activity concentration of $^{210}Pb_{ex}$ and the percentage of fine sand and mud appeared, while an inverse correlation with the bulk density of the samples was also found.

In addition, the Kruskal-Wallis test result (Table 5B) shows that

Table 4A
Spearman correlation coefficients matrix of activity concentration in Bq kg^{-1} of ^{226}Ra, ^{228}Ra, ^{40}K, $^{210}Pb_{xc}$, mean grain size in mm, sorting, percentage of coarse sand (CS), medium sand (MS), fine sand (FS), very fine sand (VFS), mud (M), depth in m and bulk density (ρ) in g cm^{-3} of samples from A) El Confital bay and B) Las Canteras beach. The p-value is set at 0.05.

A)	^{226}Ra	^{228}Ra	^{40}K	$^{210}Pb_{ex}$	Grain size	Sorting	CS	MS	FS	VFS	M	Depth	ρ
^{226}Ra	1	***0.000***	***0.000***	*0.649*	*0.572*	*0.579*	*0.594*	*0.617*	*0.770*	*0.200*	*0.770*	*0.173*	*0.333*
^{228}Ra	**0.915**	1	***0.000***	*0.471*	*0.931*	*0.778*	*0.633*	*0.339*	*0.721*	*0.362*	*0.983*	*0.191*	*0.294*
^{40}K	**0.879**	**0.979**	1	*0.405*	*0.983*	*0.854*	*0.617*	*0.269*	*0.778*	*0.387*	*1.000*	*0.150*	*0.347*
$^{210}Pb_{ex}$	−0.124	−0.194	−0.224	1	*0.068*	*0.196*	*0.060*	*0.311*	*0.610*	***0.039***	***0.012***	***0.015***	***0.000***
Grain size	−0.153	−0.024	−0.006	−0.468	1	*0.024*	*0.026*	*0.068*	*0.721*	*0.880*	*0.664*	*0.495*	*0.054*
Sorting	0.150	0.076	0.050	0.341	0.288	1	*0.176*	*0.026*	*0.068*	*0.721*	*0.880*	*0.664*	*0.495*
CS	−0.144	−0.129	−0.135	−0.479	0.768	0.356	1	*0.002*	*0.002*	*0.000*	*0.009*	*0.096*	*0.129*
MS	−0.135	−0.256	−0.294	−0.271	0.397	0.553	0.715	1	*0.105*	*0.064*	*0.274*	*0.157*	*0.276*
FS	−0.079	−0.097	−0.076	0.138	−0.818	−0.468	−0.715	−0.421	1	*0.001*	*0.001*	*0.398*	*0.461*
VFS	0.338	0.244	0.232	**0.521**	−0.918	−0.097	−0.829	−0.474	0.765	1	*0.000*	*0.020*	*0.065*
M	0.079	0.006	0.000	**0.612**	−0.868	0.041	−0.629	−0.291	0.729	0.882	1	*0.009*	*0.008*
Depth	0.358	0.345	0.377	**0.595**	−0.551	0.118	−0.430	−0.371	0.227	0.575	0.632	1	*0.008*
ρ	0.259	0.280	0.252	**−0.855**	0.490	−0.184	0.396	0.290	−0.199	−0.472	−0.640	−0.636	1

p-value 0.05.

Table 4B

B)	^{226}Ra	^{228}Ra	^{40}K	$^{210}Pb_{ex}$	Grain size	Sorting	CS	MS	FS	VFS	M	Depth	ρ
^{226}Ra	1	***0.000***	***0.000***	*0.460*	***0.004***	*0.326*	***0.012***	*0.254*	*0.761*	***0.005***	*0.450*	*0.387*	***0.017***
^{228}Ra	**0.899**	1	***0.000***	*0.340*	***0.003***	*0.383*	***0.013***	*0.270*	*0.690*	***0.004***	*0.500*	*0.220*	***0.008***
^{40}K	**0.912**	**0.942**	1	*0.100*	***0.018***	*0.975*	*0.069*	*0.446*	*0.177*	***0.001***	*0.391*	*0.297*	***0.000***
$^{210}Pb_{ex}$	0.162	0.209	0.352	1	*0.252*	***0.004***	*0.177*	*0.050*	***0.001***	*0.581*	***0.022***	*0.081*	***0.000***
Grain size	**0.573**	**0.586**	**0.489**	−0.249	1	*0.073*	*0.000*	*0.000*	*0.078*	*0.000*	*0.871*	*0.015*	*0.623*
Sorting	0.214	0.191	0.007	−0.572	0.380	1	*0.004*	*0.067*	*0.000*	*0.587*	*0.068*	*0.884*	*0.054*
CS	**0.515**	**0.509**	0.386	−0.292	0.917	0.571	1	*0.000*	*0.006*	*0.005*	*0.857*	*0.246*	*0.881*
MS	0.248	0.240	0.167	−0.413	0.828	0.388	0.840	1	*0.019*	*0.004*	*0.475*	*0.070*	*0.959*
FS	0.067	0.088	0.292	**0.639**	−0.375	−0.786	−0.551	−0.485	1	*0.565*	*0.071*	*0.936*	*0.028*
VFS	**−0.567**	**−0.582**	**−0.658**	−0.122	−0.744	0.120	−0.560	−0.581	−0.126	1	*0.719*	*0.004*	*0.009*
M	0.166	0.148	0.188	**0.474**	−0.036	−0.387	−0.040	−0.157	0.383	−0.079	1	*0.047*	*0.139*
Depth	−0.189	−0.266	−0.227	0.371	−0.501	0.032	−0.252	−0.384	0.018	0.576	0.419	1	*0.792*
ρ	**−0.492**	**−0.538**	**−0.690**	**−0.680**	−0.108	0.406	−0.033	0.011	−0.458	0.535	−0.318	0.058	1

p-value 0.05.

Table 5A
Statistical results for the identification of the presence of significant differences in the activity concentration values of the different grain size categories. The results displayed correspond to A) the One-way ANOVA test applied to the activity concentrations values of ^{226}Ra, ^{228}Ra and ^{40}K which followed a normal distribution and B) to the Kruskal-Wallis test applied to $^{210}Pb_{ex}$ since this did not follow a normal distribution. In addition, the results of the Wilcoxon rank sum test are displayed to identify the groups within which significant differences were found.

A	field	F	Prob-F
^{226}Ra	Grain size categories	0.1925	0.9010
^{228}Ra	Grain size categories	0.0749	0.9732
^{40}K	Grain size categories	0.5255	0.6668

ANOVA prob-F 0.05.

Table 5B

B	field	p-value	Wilcoxon rank sum test
$^{210}Pb_{ex}$	Grain size categories	0.0026	D - A (0.00017) D - B (0.01401)

Kruskal-Wallis p-value 0.05.

Wilcoxon rank sum test p-value 0.05.

$^{210}Pb_{ex}$ presented significant differences among the different categories. Hence, a Wilcoxon rank-sum test was applied, and the results showed that the smallest-grain-size group (category D), displayed significant differences with the larger-grain-size groups (categories A and B). These higher activity concentration values of $^{210}Pb_{ex}$ in the smallest grain size category can also be appreciated in the boxplot from Fig. 6.

All these results showed that in the whole study region, the samples that presented higher activity concentration values of $^{210}Pb_{ex}$ were those lighter and with smaller grain sizes. This relationship is similar to that found by other authors (Huang et al., 2013; Lin et al., 2020; Pappa et al., 2016; Patiris et al., 2016) and can be explained by the origin of $^{210}Pb_{ex}$. Unsupported ^{210}Pb is scavenged in small aerosol particles that reach the surface through, among other mechanisms, aeolian dust deposition. Since the particles that travel the longest distance generally present clay and silt sizes, these aerosol particles normally have small grain sizes (Lawrence and Neff, 2009; Papastefanou, 2008). Hence, what the correlation analysis is describing for the bay in the case of $^{210}Pb_{ex}$ agrees with what could be expected for $^{210}Pb_{ex}$ considering its origin.

4.3. Mineral composition of sand samples

The mineralogical content of 6 samples was analysed to try to identify the minerals that could be responsible for the activity concentration values of ^{226}Ra, ^{228}Ra and ^{40}K. The samples correspond to two samples from the high-activity part of the bay (D7 and D8) and two from the low-activity part of the bay (D15 and D19). Furthermore, one sample from the high-activity area (S3) and one sample from the low-activity area (S8) of the submerged part of the beach were also analysed. The intertidal zone of Las Canteras Beach was studied and described in an earlier work (Arriola-Velásquez et al., 2021) and thus, the results of this study could be compared to previous results.

The results of the XRPD analysis and the activity concentration values of ^{226}Ra, ^{228}Ra and ^{40}K for each sample are shown in Table 6. The SCXRD analysis determined that the feldspar is anorthoclase ($Ab_{0.83}Or_{0.16}An_{0.01}$), the clinopyroxene is Fe-rich diopside and the amphibole is potassic-pargasite (cell parameters are a = 9.8449(3), b = 18.0554(4), c = 5.3090(2) Å, α = 90°, β = 105.509(3)°, γ = 90°, V =

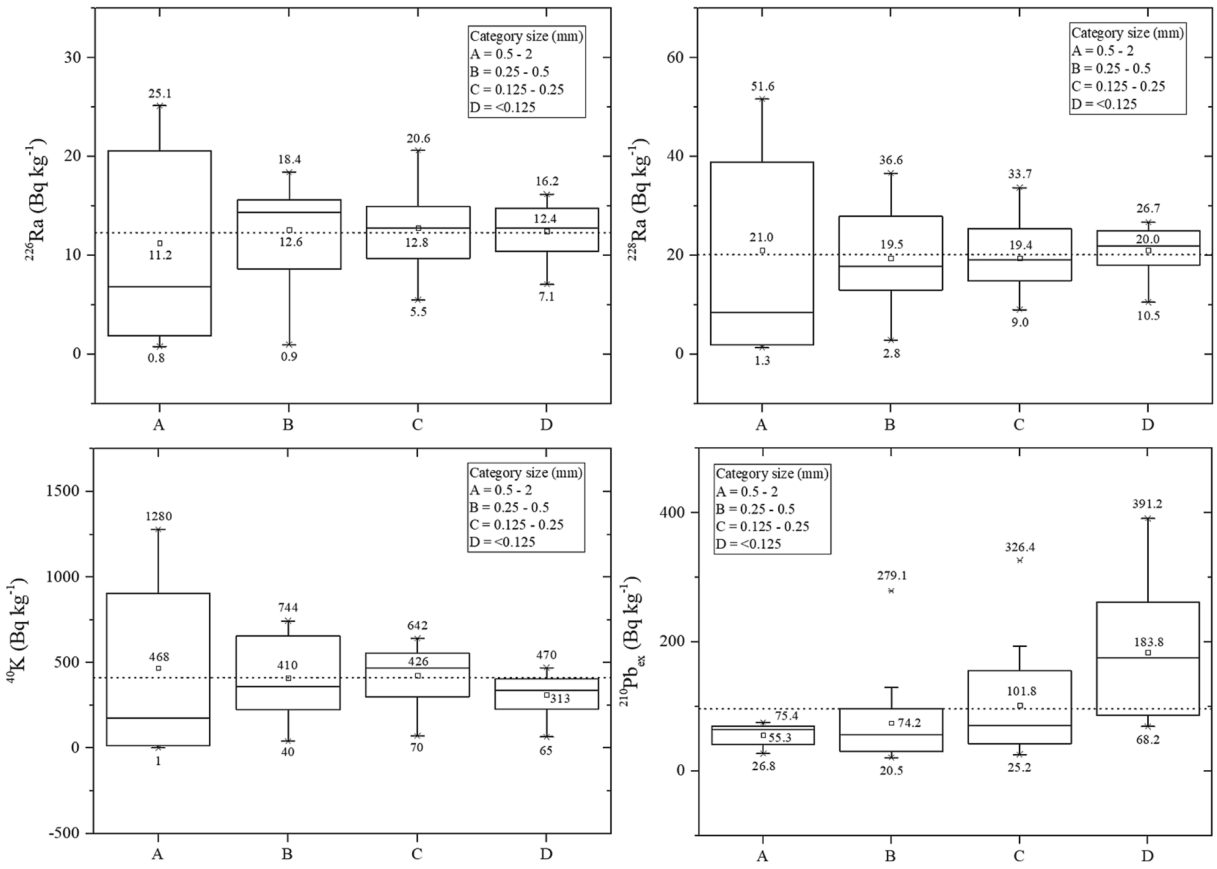

Fig. 6. Boxplots of the activity concentration values of ^{226}Ra, ^{228}Ra, ^{40}K and ^{210}Pb$_{ex}$ found for the different grain size fractions in El Confital bay and Las Canteras beach. The dot line indicates the mean activity concentration value of each radionuclide. The numbers that appear in each whisker correspond to the maximum and minimum activity concentration values. The number in the middle indicates the mean activity concentration value for each grain size category.

909.33(5) Å^3). Table 6 also includes the sum of biogenic carbonate, which was obtained by adding the percentages of calcite and aragonite. In addition, the sum of feldspars, feldspathoids and zeolites is also displayed. This last sum includes the percentages of labradorite, anorthoclase, sanidine, analcime, nepheline, phillipsite and fluorapatite.

The sample that presented the lowest amount of feldspars, feldspathoids and zeolites was sample D15, which was also the sample with the lowest activity concentration values of ^{40}K. In contrast, the sample with the highest activity concentration values of these radionuclides was sample D7, which presented the highest amount of feldspars, feldspathoids and zeolites. Considering that the main source of potassium identified in the samples is the group of feldspars, feldspathoids and zeolites, it seems that the increase in the activity concentration of ^{40}K is related to an increase in the content of these minerals in the samples. This idea was also suggested in an earlier study that was carried out on Las Canteras Beach (Arriola-Velásquez et al., 2021). According to these authors, the samples from the intertidal part of the beach that was completely exposed to wave action showed a decrease in the potassium feldspar content during erosion periods and an increase in the amount of these minerals during accumulation periods. In the protected area of the beach, these minerals were always present. Therefore, in this previous work, the increase in the activity concentration of ^{40}K was associated with the transport and accumulation of these K-feldspars. Moreover, in other parts of the world with sediments of volcanic origin, other authors also found that an increase in the activity concentration values of ^{40}K was associated with an increase in the feldspar content in the samples (Roviello et al., 2020). All of this seems to agree with what was found in this work, although in some of the results obtained here, other minerals like amphibole also contribute to the amount of potassium present in the samples. Nevertheless, the results seem to confirm that higher activity concentration values of ^{40}K are associated with a larger amount of potassium-bearing minerals in the samples.

Regarding the organic materials, at first, it seemed that the lower activity concentration values appeared in the samples with a higher biogenic carbonate content, as in the case of sample D15, which was 97.4 % biogenic carbonate. However, there are other samples, such as S3 and D19, in which the organic carbonate contents are similar, but one sample presents more than double the activity concentration value of ^{40}K of the other. Therefore, the biogenic content of the samples does not seem to influence the activity concentration value of ^{40}K in the samples. In fact, considering what was mentioned before, in the case of sample S3, the content of K-bearing minerals is 25.7 %, while for D19, it is 12.9 %. This again reinforces the idea that the activity concentration values found for ^{40}K in the samples are more associated with its terrigenous content, and there is no influence of the organic material.

The results of the mineralogical analysis showed that ^{40}K acts as a good tracer of the transport and accumulation of sediments due to its K-bearing minerals. Nevertheless, even though no Ra-bearing minerals were found in the study region, ^{226}Ra and ^{228}Ra follow a pattern similar to that followed by ^{40}K in all samples. These similarities between radium and potassium were also found in the work of Arriola-Velásquez et al. (2021). In different coordination environments, both potassium and radium present similar ionic radii (Shannon, 1976), which could favour the entrance of Ra in the K-feldspars. However, no data on this are available in this study region, and further studies would be necessary to better understand the reasons that ^{226}Ra and ^{228}Ra behave in the same way as ^{40}K.

Table 6
Results of quantitative analysis of mineralogical composition on the studied sand samples in percentage. The results include the sum of the percentage of feldspars, feldspathoids and zeolites of the samples (Σ Fdp + zeolites) and the sum of the percentage of biogenic carbonates (Σ Biogenic carbonates). The activity concentration values of ^{226}Ra, ^{228}Ra and ^{40}K for each sample is given in Bq kg^{-1}.

	S3	S8	D7	D8	D15	D19
Calcite ($CaCO_3$)	40.9 ± 0.5	12.5 ± 0.3	1.9 ± 0.2	13.7 ± 0.4	80.1 ± 0.2	44.6 ± 0.4
Aragonite ($CaCO_3$)	11.0 ± 0.3	6.7 ± 0.2	1.6 ± 0.3	–	17.3 ± 0.2	15.9 ± 0.3
Augite (Ca(Mg,Fe,Al)Si_2O_6)	18.0 ± 0.5	61.3 ± 0.6	17.8 ± 0.5	20.1 ± 0.5	–	16.2 ± 0.5
Amphibole (potassic-pargasite, $KCa_2(Mg_4Al)(Si_6Al_2)O_{22}(OH)_2$)	–	5.1 ± 0.2	–	–	–	–
Forsteritic olivine	–	6.6 ± 0.4	–	–	–	–
Cristobalite (SiO_2)	1.1 ± 0.1	0.8 ± 0.1	0.9 ± 0.1	1.2 ± 0.1	–	–
α-quartz (SiO_2)	–	–	–	1.2 ± 0.2	–	–
Haematite (Fe_2O_3)	–	–	1.4 ± 0.1	1.5 ± 0.2	–	–
Labradorite ($(Na_x,Ca_{1-x})(Al_{1+x}Si_{3-x})O_8$)	3.2 ± 0.2	0.9 ± 0.1	19.7 ± 0.6	15.0 ± 0.7	–	8.6 ± 0.4
Anorthoclase ($(Na_x,K_{1-x})(AlSi_3)O_8$)	15.9 ± 0.6	6.1 ± 0.4	32.1 ± 0.7	20.0 ± 0.6	–	4.1 ± 0.4
Sanidine ($KAlSi_3O_8$)*	9.8 ± 0.5	–	18.2 ± 0.6	13.2 ± 0.5	2.6 ± 0.2	3.1 ± 0.3
Analcime ($NaAlSi_2O_6{\cdot}H_2O$)	–	–	2.8 ± 0.2	2.2 ± 0.2	–	1.8 ± 0.2
Nepheline ($Na_3KAl_4Si_4O_{16}$)	–	–	3.5 ± 0.4	–	–	–
Phillipsite ($(CaNa_2K_2)Al_6Si_{10}O_{32}{\cdot}12H_2O$)	–	–	–	10.4 ± 0.6	–	5.7 ± 0.4
Fluorapatite ($Ca_4(PO_4)_3(F_2)$)	–	–	–	1.5 ± 0.3	–	–
Σ Biogenic carbonates	51.9 %	19.2 %	3.5 %	13.7 %	97.4 %	60.5 %
Σ Fdp + zeolites	28.9 %	7.0 %	76.3 %	62.3 %	2.6 %	23.3 %
^{40}K	490 ± 20	119 ± 8	940 ± 40	580 ± 30	37 ± 7	150 ± 10
^{226}Ra	14 ± 1	7.4 ± 0.7	25 ± 1	18 ± 1	<MDA (2.9)	12.7 ± 0.9
^{228}Ra	20 ± 2	10 ± 1	41 ± 3	30 ± 2	<MDA (2.8)	10 ± 2

* Or polymorph (orthoclase, microcline).

5. Conclusions

For both campaigns, 2005/2006 and 2022, higher and lower ^{226}Ra, ^{228}Ra and ^{40}K activity concentrations were found respectively in the western and eastern sediments of El Confital Bay. These values were mainly related to sediment mineralogy. Additionally, a transport of sediments from the west coastline to the deeper parts of the bay was seemingly traced by ^{226}Ra, ^{228}Ra and ^{40}K highest activity concentration values when the two campaigns were compared.

The spatial distribution of the ^{226}Ra, ^{228}Ra and ^{40}K activity concentration values also seemed to be tracing the sediment dynamics that occur in the submerged part of Las Canteras Beach. Lower values were found where erosion processes are more frequent, in the open part of the submerged beach, while the accumulation zone in the protected area of the submerged beach presented higher values. Furthermore, the progressive increase of activity concentrations from the erosion to the accumulation areas appears to trace the longshore sediment transport that occurs on the beach.

The spatial distribution of the activity concentration of ^{210}Pb$_{ex}$ can be used to identify areas where accumulation due to particle sedimentation is favoured. Sediments from the deeper areas of El Confital Bay and sheltered parts of the submerged zone of Las Canteras Beach presented higher ^{210}Pb$_{ex}$ activity concentrations. Conversely, lower activity concentration values were found in the shallower parts of the bay and open part of the beach, where more seabed erosion occurs. In addition, higher ^{210}Pb activity concentration values were related to smaller grain size sediment fractions, which agrees with the origin of unsupported ^{210}Pb adsorbed to atmospheric aerosols. Further studies including analysis of vertical profiles of ^{210}Pb$_{ex}$ in the sediment column would be necessary to better comprehend its role as a tracer of these sedimentation areas.

Overall, this work identifies as tracers of sediment dynamics some natural radionuclides that are part of the coastal system under study, considering a variability analysis of their activity concentrations with local sediment characteristics (such as grain size or mineralogical composition), as well as with sediment transport. Therefore, the present paper establishes a basis for studies of sediment erosion and accumulation processes in coastal systems using natural radiotracers, including those studies based on emerging methodologies of mapping using in situ gamma spectroscopy. In addition, because the coastal system studied includes the opposing dynamic of a beach open to the wave action and a beach protected against it, the results and methods developed can be extrapolated to different parts of the world.

Declaration of Competing Interest

The authors declare that they have no known competing financial interests or personal relationships that could have appeared to influence the work reported in this paper.

Data availability

Data will be made available on request.

Acknowledgements

This work was partially supported by the Consejería de Economía, Industria, Comercio y Conocimiento del Gobierno de Canarias. F.C. and M.C. acknowledge financial support from the Italian Ministry of Education (MUR) through the project “Dipartimenti di Eccellenza 2023–2027”. The authors are grateful to the anonymous reviewers and editor for their professional and meticulous evaluation and the International Atomic Energy Agency for all the discussions and suggestions made through the Coordinated Research Project F22074, “Development of Radiometric Methods and modelling for measurement of sediment transport in coastal systems and rivers”.

Appendix A. Supplementary data

Supplementary data to this article can be found online at https://doi.org/10.1016/j.catena.2023.107672.

References

Achilleos, G.A., 2011. The Inverse Distance Weighted interpolation method and error propagation mechanism – creating a DEM from an analogue topographical map. J. Spat. Sci. 56, 283–304. https://doi.org/10.1080/14498596.2011.623348.

Alfonso, J.A., Pérez, K., Palacios, D., Handt, H., LaBrecque, J.J., Mora, A., Vásquez, Y., 2014. Distribution and environmental impact of radionuclides in marine sediments along the Venezuelan coast. J. Radioanal. Nucl. Chem. 300, 219–224. https://doi.org/10.1007/s10967-014-2999-z.

Alonso, I., 1993. Procesos sedimentarios en la playa de Las Canteras (Gran Canaria). Universidad de Las Palmas de Gran Canaria, Las Palmas de Gran Canaria.

Alonso, I., 2005. Costa Norte: Playa De Las Canteras. In: Hernández, L., Alonso, I., Mangas, J., Yanes, A. (Eds.), Tendencias Actuales En Geomorfología Litoral. Universidad de Las Palmas de Gran Canaria, La Palmas de Gran Canaria, pp. 219–238.

Alonso, I., Pérez Torrado, F.J., 1992. Estudio sedimentológico de la playa de Las Canteras (Gran Canaria). Datos preliminares. III Congreso Geológico De España y Tomo 2, 131–135.

Alonso, I., Vilas, F., 1996. Variabilidad sedimentaria en la playa de Las Canteras (Gran Canaria). Geogaceta 20, 428–430.
Alveirinho Dias, J., 2004. A análise sedimentar e o conhecimento dos sistemas marinhos: uma introdução à oceanografia geológica, First. ed. Universidade do Algarve, Faro.
Androulakaki, E.G., Tsabaris, C., Eleftheriou, G., Kokkoris, M., Patiris, D.L., Vlastou, R., 2015. Seabed radioactivity based on in situ measurements and Monte Carlo simulations. Appl. Radiat. Isot. 101, 83–92. https://doi.org/10.1016/j.apradiso.2015.03.013.
Arnedo, M.A., Tejera, A., Rubiano, J.G., Alonso, H., Gil, J.M., Rodríguez, R., Martel, P., 2013. Natural radioactivity measurements of beach sands in gran Canaria, Canary Islands (Spain). Radiat. Prot. Dosim. 156, 75–86. https://doi.org/10.1093/rpd/nct044.
Arnedo, M.A., Rubiano, J.G., Alonso, H., Tejera, A., González, A., González, J., Gil, J.M., Rodríguez, R., Martel, P., Bolivar, J.P., 2017. Mapping natural radioactivity of soils in the eastern Canary Islands. J. Environ. Radioact. 166, 242–258. https://doi.org/10.1016/j.jenvrad.2016.07.010.
Arriola-Velásquez, A., Tejera, A., Guerra, J.G., Alonso, I., Alonso, H., Arnedo, M.A., Rubiano, J.G., Martel, P., 2019. Spatio-temporal variability of natural radioactivity as tracer of beach sedimentary dynamics. Estuar. Coast. Shelf Sci. 231 https://doi.org/10.1016/j.ecss.2019.106476.
Arriola-Velásquez, A.C., Tejera, A., Guerra, J.G., Geibert, W., Stimac, I., Cámara, F., Alonso, H., Rubiano, J.G., Martel, P., 2021. ^{226}Ra, ^{228}Ra and ^{40}K as tracers of erosion and accumulation processes: A 3-year study on a beach with different sediment dynamics. Catena (amst) 207, 105705. https://doi.org/10.1016/j.catena.2021.105705.
Balcells, R., Barrera, J.L., Ruiz García, M.T., (Cartographers), 1990. Geological Map 1101-I-II Las Palmas de Gran Canaria, 1:25000 IGME.
Bezuidenhout, J., 2013. Measuring naturally occurring uranium in soil and minerals by analysing the 352keV gamma-ray peak of 214Pb using a NaI(Tl)-detector. Appl. Radiat. Isot. 80, 1–6. https://doi.org/10.1016/j.apradiso.2013.05.008.
Bezuidenhout, J., 2020. The investigation of natural radionuclides as tracers for monitoring sediment processes. J Appl Geophy 181, 104135. https://doi.org/10.1016/j.jappgeo.2020.104135.
Blott, S.J., Pye, K., 2001. Gradistat : a grain size distribution and statistics package for the analysis of unconsolidated sediments. Earth Surf. Proc. Land. 26, 1237–1248. https://doi.org/10.1002/esp.261.
Bobos, I., Madruga, M.J., Reis, M., Esteves, J., Guimarães, V., 2021. Clay mineralogy insights and assessment of the natural (228Ra, 226Ra, 210Pb, 40K) and anthropogenic (137Cs) radionuclides dispersion in the estuarine and lagoon systems along the Atlantic coast of Portugal. Catena (amst) 206, 105532. https://doi.org/10.1016/j.catena.2021.105532.
Charkin, A.N., Yaroshchuk, E.I., Dudarev, O., v., Leusov, A.E., Goriachev, V.A., Sobolev, I.S., Gulenko, T.A., Pipko, I.I., Startsev, A.M., Semiletov, I.P., 2022. The influence of sedimentation regime on natural radionuclide activity concentration in marine sediments of the East Siberian Arctic Shelf. J. Environ. Radioact. 253–254 https://doi.org/10.1016/j.jenvrad.2022.106988.
Chiozzi, P., Pasquale, V., Verdoya, M., Minato, S., 2001. Natural gamma-radiation in the Aeolian volcanic arc. Appl. Radiat. Isot. 55, 737–744.
Cooper, L.W., Grebmeier, J.M., 2018. Deposition patterns on the Chukchi shelf using radionuclide inventories in relation to surface sediment characteristics. Deep Sea Res 2 Top Stud Oceanogr 152, 48–66. https://doi.org/10.1016/j.dsr2.2018.01.009.
Dueñas, C., Gordo, E., Liger, E., Cabello, M., Cañete, S., Pérez, M., de la Torre-Luque, P., 2017. ^{7}Be, ^{210}Pb and ^{40}K depositions over 11 years in Málaga. J. Environ. Radioact. 178–179, 325–334. https://doi.org/10.1016/j.jenvrad.2017.09.010.
Eulie, D.O., Corbett, D.R., Walsh, J.P., 2018. Shoreline erosion and decadal sediment accumulation in the Tar-Pamlico estuary, North Carolina, USA: A source-to-sink analysis. Estuar. Coast. Shelf Sci. 202, 246–258. https://doi.org/10.1016/j.ecss.2017.10.011.
Feng, H., Zhang, W., Jia, L., Weinstein, M.P., Zhang, Q., Yuan, D., Tao, J., Yu, L., 2010. Short- and long-term sediment transport in western Bohai Bay and coastal areas. Chin. J. Oceanol. Limnol. 28, 583–592. https://doi.org/10.1007/s00343-010-9099-x.
Fernández-Aldecoa, J.C., Robayna, B., Allende, A., Poffijn, A., Hernández-Armas, J., 1992. Natural radiation in Tenerife (Canary Islands). Radiat. Prot. Dosim. 45, 545–548.
Folk, R.L., Ward, W.C., 1957. Brazos River Bar: A study in the significance of grain size parameters. J. Sediment. Petrol. 27, 3–26.
Froehlich, K., 2010. Environmental radionuclides: Tracers and Timers of Terrestrial Processes, First. ed. Elsevier B.V., Amsterdam. https://doi.org/10.1016/S1569-4860(09)01613-1.
Gaspar, L., Webster, R., Navas, A., 2017. Fate of $^{210}Pb_{ex}$ fallout in soil under forest and scrub of the central Spanish Pre-Pyrenees. Eur. J. Soil Sci. 68, 259–269. https://doi.org/10.1111/ejss.12427.
Gong, G., Mattevada, S., O'Bryant, S.E., 2014. Comparison of the accuracy of kriging and IDW interpolations in estimating groundwater arsenic concentrations in Texas. Environ. Res. 130, 59–69. https://doi.org/10.1016/j.envres.2013.12.005.
Gordo, E., Liger, E., Dueñas, C., Fernández, M.C., Cañete, S., Pérez, M., 2015. Study of 7Be and 210Pb as radiotracers of African intrusions in Malaga (Spain). J. Environ. Radioact. 148, 141–153. https://doi.org/10.1016/j.jenvrad.2015.06.028.
Gražulis, S., Chateigner, D., Downs, R.T., Yokochi, A.F.T., Quirós, M., Lutterotti, L., Manakova, E., Butkus, J., Moeck, P., le Bail, A., 2009. Crystallography Open Database - An open-access collection of crystal structures. J. Appl. Cryst. 42, 726–729. https://doi.org/10.1107/S0021889809016690.
Gu, F., Zhang, X., Ren, B., Zhou, M., 2022. A new approach for dating recent silting soils of debris flow deposits from the changes of $^{210}Pb_{ex}$ concentration in surface layers. Catena (amst) 214. https://doi.org/10.1016/j.catena.2022.106254.
Guerra, J.G., Rubiano, J.G., Winter, G., Guerra, A.G., Alonso, H., Arnedo, M.A., Tejera, A., Gil, J.M., Rodríguez, R., Martel, P., Bolivar, J.P., 2015. A simple methodology for characterization of germanium coaxial detectors by using Monte Carlo simulation and evolutionary algorithms. J. Environ. Radioact. 149, 8–18. https://doi.org/10.1016/j.jenvrad.2015.06.017.
Guerra, J.G., Rubiano, J.G., Winter, G., Guerra, G., A., Alonso, H., Arnedo, M.A., Tejera, A., Martel, P., Bolivar, J.P., 2017. Computational characterization of HPGe detectors usable for a wide variety of source geometries by using Monte Carlo simulation and a multi-objective evolutionary algorithm. Nucl. Instrum. Methods Phys. Res. A 858, 113–122. https://doi.org/10.1016/j.nima.2017.02.087.
Hallermeier, R.J., 1981. A profile zonation for seasonal sand beaches from wave climate. Coast. Eng. 4, 253–277.
Huang, D., Du, J., Deng, B., Zhang, J., 2013. Distribution patterns of particle-reactive radionuclides in sediments off eastern Hainan Island, China: Implications for source and transport pathways. Cont. Shelf Res. 57, 10–17. https://doi.org/10.1016/j.csr.2012.04.019.
Hülse, P., Bentley, S.J., 2012. A 210Pb sediment budget and granulometric record of sediment fluxes in a subarctic deltaic system: The Great Whale River, Canada. Estuar. Coast. Shelf Sci. 109, 41–52. https://doi.org/10.1016/j.ecss.2012.05.019.
Iaea, 2012. Worldwide Open Proficiency Test: Determination of Natural and Artificial Radionuclides in Moss-Soil and Water. IAEA Analytical Quality in Nuclear Applications Series, IAEA, Vienna.
International Atomic Energy Agency, 2014. Radiotracer and Sealed Source Applications in Sediment Transport Studies, Training Course Series No. 59. IAEA, Vienna.
Kilel, K.K., Bezuidenhout, J., Gatari, M.J., le Roux, R.R., Kaniu, M.I., 2022. A low-cost delta underwater gamma system (DUGS) for in-situ measurement of natural radionuclides in aquatic sediments. J. Radioanal. Nucl. Chem. https://doi.org/10.1007/s10967-022-08701-7.
Lawrence, C.R., Neff, J.C., 2009. The contemporary physical and chemical flux of aeolian dust: A synthesis of direct measurements of dust deposition. Chem. Geol. 267, 46–63. https://doi.org/10.1016/j.chemgeo.2009.02.005.
Ligero, R.A., Ramos-Lerate, I., Barrera, M., Casas-Ruiz, M., 2001. Relationships between sea-bed radionuclide activities and some sedimentological variables. J. Environ. Radioact. 57, 7–19.
Lin, W., Feng, Y., Yu, K., Lan, W., Wang, Y., Mo, Z., Ning, Q., Feng, L., He, X., Huang, Y., 2020. Long-lived radionuclides in marine sediments from the Beibu Gulf, South China Sea: Spatial distribution, controlling factors, and proxy for transport pathway. Mar. Geol. 424, 106157 https://doi.org/10.1016/j.margeo.2020.106157.
López-Pérez, M., Lorenzo-Salazar, J.M., Expósito, F.J., Díaz, J.P., Salazar, P., 2020. Impact of a massive dust storm on the gross alpha, gross beta, ^{40}K, ^{137}Cs, ^{210}Pb, ^{7}Be activities measured in atmospheric aerosols collected in Tenerife, Canary Islands. Atmos. Environ. 239, 117806 https://doi.org/10.1016/j.atmosenv.2020.117806.
Madruga, M.J., Silva, L., Gomes, A.R., Libânio, A., Reis, M., 2014. The influence of particle size on radionuclide activity concentrations in Tejo River sediments. J. Environ. Radioact. 132, 65–72. https://doi.org/10.1016/j.jenvrad.2014.01.019.
Mangas, J., Julià-Miralles, M., 2015. Geomorfología y naturaleza de las bajas submareales de Bajo Fernando, Los Roquerillos y La Zabala (NE de Gran Canaria). Geo-Temas 15, 37–40.
Medina, R., Bastón, S., Cánovas, V., Torres, A., Luque, Á., Alonso, I., Sánchez, I., Ortega, A., Rodríguez, S., Martín, J.A., 2006. Estudio integral de la playa de Las Canteras, Technical Report Dirección General de Costas.
Mtshawu, B., Bezuidenhout, J., Kilel, K.K., 2023. Spatial autocorrelation and hotspot analysis of natural radionuclides to study sediment transport. J. Environ. Radioact. 264 https://doi.org/10.1016/j.jenvrad.2023.107207.
Papastefanou, C., 2008. Radioactive aerosols, First. ed. Radioactivity in the Environment. Elsevier B. V, Amsterdam.
Pappa, F.K., Tsabaris, C., Ioannidou, A., Patiris, D.L., Kaberi, H., Pashalidis, I., Eleftheriou, G., Androulakaki, E.G., Vlastou, R., 2016. Radioactivity and metal concentrations in marine sediments associated with mining activities in Ierissos Gulf, North Aegean Sea, Greece. Appl. Radiat. Isot. 116, 22–33. https://doi.org/10.1016/j.apradiso.2016.07.006.
Patiris, D.L., Tsabaris, C., Anagnostou, C.L., Androulakaki, E.G., Pappa, F.K., Eleftheriou, G., Sgouros, G., 2016. Activity concentration and spatial distribution of radionuclides in marine sediments close to the estuary of Shatt al-Arab/Arvand Rud River, the Gulf. J. Environ. Radioact. 157, 1–15. https://doi.org/10.1016/j.jenvrad.2016.02.025.
Ramadan, A.A., Diab, H.M., 2013. Radiological characterization and environmental impact in northwestern coast of Egypt. J. Radioanal. Nucl. Chem. 89–95. https://doi.org/10.1007/s10967-012-2091-5.
Rosner, B., Glynn, R.J., 2009. Power and sample size estimation for the wilcoxon rank sum test with application to comparisons of C statistics from alternative prediction models. Biometrics 65, 188–197. https://doi.org/10.1111/j.1541-0420.2008.01062.x.
Roviello, V., De Cesare, M., D'Onofrio, A., Gialanella, L., Guan, Y.J., Roos, P., Ruberti, D., Sabbarese, C., Terrasi, F., 2020. New analytical methods for the assessment of natural (238U, 232Th, 226Ra, 40K) and anthropogenic (137Cs) radionuclides as actinides (239Pu, 240Pu): The case study of the Garigliano NPP releases along the Domitia sandy beaches (Southern Italy). Catena (amst) 193, 104612. https://doi.org/10.1016/j.catena.2020.104612.
Schmincke, H.U., 1993. Geological field guide of Gran Canaria, 6th ed. Pluto-Press, Kiel (Germany).
Shannon, R.D., 1976. Revised Effective Ionic Radii and Systematic Studies of Interatomic Distances in Halides and Chaleogenides. Acta Crystallographica Section A 32, 751–767.
Shapiro, S.S., Wilk, M.B., 1965. An Analysis of Variance Test for Normality (Complete Samples). Biometrika 52, 591–611. https://doi.org/10.2307/2333709.

Sheldrick, G.M., 2015. Crystal structure refinement with SHELXL. Acta Crystallogr C Struct Chem 71, 3–8. https://doi.org/10.1107/S2053229614024218.

Theodorsson-Norheim, E., 1986. Kruskal-Wallis test: BASIC computer program to perform nonparametric one-way analysis of variance and multiple comparisons on ranks of several independent samples. Comput. Methods Programs Biomed. 23, 57–62. https://doi.org/10.1016/0169-2607(86)90081-7.

Thereska, J., 2009. Natural radioactivity of coastal sediments as tracer in dynamic sedimentology. Nukleonika 54, 45–50.

Toby, B.H., von Dreele, R.B., 2013. GSAS-II: The genesis of a modern open-source all purpose crystallography software package. J. Appl. Cryst. 46, 544–549. https://doi.org/10.1107/S0021889813003531.

Tsabaris, C., Evangeliou, N., Fillis-Tsirakis, E., Sotiropoulou, M., Patiris, D.L., Florou, H., 2012. Distribution of natural radioactivity in sediment cores from Amvrakikos Gulf (western Greece) as a part of IAEA's campaign in the Adriatic and Ionian seas. Radiat. Prot. Dosim. 150, 474–487. https://doi.org/10.1093/rpd/ncr436.

Tsabaris, C., Patiris, D., Maramathas, C., Androulakaki, E., Eleftheriou, G., Pappa, F., Alexakis, S., 2023a. Surveillance of the seashore using the KATERINA II geo-referenced detection system. HNPS Advances in Nuclear Physics 29, 137–143. https://doi.org/10.12681/hnpsanp.2473.

Tsabaris, C., Patiris, D.L., Adams, R., Castillo, J., Henriquez, M.F., Hurtado, C., Munoz, L., Kalpaxis, L., Verri, M., Alexakis, S., Pappa, F.K., Lampousis, A., 2023b. In situ radioactivity maps and trace metal concentrations in beach sands of a mining coastal area at North Aegean, Greece. J. Mar. Sci. Eng. 11, 1207. https://doi.org/10.3390/jmse11061207.

Williams, L.J., Abdi, H., 2010. Tukey 's honestly signiflcant difference test (HSD). Encyclopedia of Research Design 2–7.

Zebracki, M., Eyrolle-Boyer, F., Evrard, O., Claval, D., Mourier, B., Gairoard, S., Cagnat, X., Antonelli, C., 2015. Tracing the origin of suspended sediment in a large Mediterranean river by combining continuous river monitoring and measurement of artificial and natural radionuclides. Sci. Total Environ. 502, 122–132. https://doi.org/10.1016/j.scitotenv.2014.08.082.